COUP census of X-ray stars in BN-KL and OMC-1S

Nicolas Grosso, Eric D. Feigelson, Konstantin V. Getman, Leisa Townsley, Patrick Broos, Ettore Flaccomio, Mark J. Mccaughrean, Giuseppina Micela, Salvatore Sciortino, John Bally, et al.

▶ **To cite this version:**

Nicolas Grosso, Eric D. Feigelson, Konstantin V. Getman, Leisa Townsley, Patrick Broos, et al.. COUP census of X-ray stars in BN-KL and OMC-1S. Astronomy and Astrophysics Supplement Series, 2005, 160, pp.530-556. 10.1086/432101 . hal-00004642

HAL Id: hal-00004642
https://hal.science/hal-00004642

Submitted on 6 Apr 2005

HAL is a multi-disciplinary open access archive for the deposit and dissemination of scientific research documents, whether they are published or not. The documents may come from teaching and research institutions in France or abroad, or from public or private research centers.

L'archive ouverte pluridisciplinaire **HAL**, est destinée au dépôt et à la diffusion de documents scientifiques de niveau recherche, publiés ou non, émanant des établissements d'enseignement et de recherche français ou étrangers, des laboratoires publics ou privés.

Chandra Orion Ultradeep Project census of X-ray stars in the BN-KL and OMC-1S regions

N. Grosso[1], E. D. Feigelson[2], K. V. Getman[2], L. Townsley[2], P. Broos[2], E. Flaccomio[3], M. J. McCaughrean[4,5], G. Micela[3], S. Sciortino[3], J. Bally[6], N. Smith[6], A. A. Muench[7], G. P. Garmire[2], F. Palla[8]

ABSTRACT

We present a study of the X-ray sources detected in the vicinity of two density peaks in the Orion Molecular Cloud 1 (OMC-1) behind the Orion Nebula Cluster (ONC), as seen in the exceptionally deep (~ 10 days) exposure of the *Chandra* Orion Ultradeep Project (COUP). We focus on a $40'' \times 50''$ region around the Becklin-Neugebauer object and Kleinmann-Low nebula (collectively BN-KL) and a $60'' \times 75''$ region around OMC-1S, a secondary star-forming peak some $90''$ south of BN-KL. Forty-three and sixty X-ray sources were detected in BN-KL and OMC-1S, respectively, of which half and one-third, respectively, were found to be foreground members of the ONC, while the remaining sources are identified as obscured X-ray sources with column densities $22 \lesssim \log(N_{\rm H}/{\rm cm}^{-2}) \lesssim 24$. All but 5 and 18 of these sources have near-infrared stellar counterparts, and 22 of these appear to be young stellar objects (YSOs). X-ray sources are found close to four luminous mid-IR sources namely BN, IRc3-i2, IRc2-C, and Source n; their X-ray variability and spectral properties are typical of coronal activity in low-mass stars rather than wind emission from massive stars, suggesting that the X-ray emission may be arising from companions. The X-ray light

[1]Laboratoire d'Astrophysique de Grenoble, Université Joseph-Fourier, F-38041 Grenoble cedex 9, France; Nicolas.Grosso@obs.ujf-grenoble.fr

[2]Department of Astronomy and Astrophysics, Pennsylvania State University, 525 Davey Laboratory, University Park, PA 16802

[3]INAF, Osservatorio Astronomico di Palermo, Piazza del Parlamento 1, 90134 Palermo, Italy

[4]School of Physics, University of Exeter, Stocker Road, Exeter EX4 4QL, Devon, UK

[5]Astrophysikalisches Institut Potsdam, An der Sternwarte 16, D-14482 Potsdam, Germany

[6]Center for Astrophysics and Space Astronomy, University of Colorado at Boulder, CB 389, Boulder, CO 80309

[7]Harvard-Smithsonian Center for Astrophysics, 60 Garden Street, Cambridge, MA 02138, USA

[8]Osservatorio Astrofisico di Arcetri, Largo Enrico Fermi 5, 50125 Firenze, Italy

curve of the X-ray source close to BN shows a periodicity of ∼8.3 days and from an X-ray image deconvolution of the region around BN, we conclude that either BN itself or a low mass companion with a projected separation of ≃ 200 AU was detected. On the other hand, no emission is seen from the bright radio Source I, held by some to be the main source of luminosity in BN-KL. In OMC-1S, *Chandra* unveils a new subcluster of seven YSOs without infrared counterparts. We compare the hard band X-ray luminosity functions of obscured X-ray sources in BN-KL and OMC-1S with unobscured X-ray sources in the ONC, and estimate that the true population of obscured sources in BN-KL and OMC-1S is ≃ 46 and 57 stars, with 90% confidence intervals of 34–71 and 42–82 stars, respectively.

Subject headings: Open clusters and association: individual: BN-KL, OMC-1S – X-rays: stars – Infrared: stars individual: BN object – Stars: pre-main sequence – Stars: flare

1. Introduction

The nearest ($d \sim 450$ pc) massive molecular cloud to the Sun is the Orion Molecular Cloud 1 (henceforth OMC-1; Genzel & Stutzki 1989). OMC-1 lies immediately behind the young (1 Myr) Orion Nebula Cluster (ONC) centered on the bright Trapezium OB stars, and the Orion Nebula H II region is a thin concave blister on the facing side of the cloud (O'Dell 2001).

At its highest density peak, just ∼ 0.1 pc northwest of the Trapezium, OMC-1 hosts the closest known region of high-mass star formation, with a total infrared luminosity of $\sim 10^5\,L_\odot$ (Werner et al. 1976; Genzel & Stutzki 1989, and references therein) reprocessed and emitted by dust grains. The dominant underlying source of this large luminosity remains the subject of debate (Greenhill et al. 2004), but the region also includes a number of embedded luminous young stars such as the $\sim 10^4\,L_\odot$ Becklin-Neugebauer object (Becklin & Neugebauer 1967, henceforth BN) and several $\sim 10^3\,L_\odot$ stars (Gezari et al. 1998, and references therein). Three of these luminous infrared sources (BN, IRc2, and Source n) are associated with compact thermal radio sources indicative of ultracompact H II regions or stellar winds, and/or maser outflows (Greenhill et al. 2004, and references therein). The cluster also illuminates the extended Kleinmann-Low nebula (Kleinmann & Low 1967, henceforth KL) and powers strong shocked molecular outflows emanating from the region (Allen & Burton 1993). Combined, BN-KL is the densest and most chemically-rich region in the entire Orion giant molecular cloud complex and is the nearest and best-studied molecular hot cores. Nevertheless, despite decades of multiwavelength studies, the region is far from fully understood due to its extreme complexity.

The second density peak in OMC-1 of interest here is OMC-1S, located about 90″ south of BN-KL. OMC-1S has roughly 10% of the luminosity of BN-KL, with $L_{\rm bol} \sim 10^4\,{\rm L}_\odot$ (Mezger et al. 1990). It has long been known that the region hosts a number of deeply embedded near- and mid-infrared sources (McCaughrean 1988), and there are also several collimated molecular outflows and a number of optical Herbig-Haro objects seen in the region (see, e.g., O'Dell 2001). Based on a proper motion study of the HH objects, O'Dell & Doi (2003) proposed them all have the same origin which he termed the Optical Outflow Source (OOS), although it seems more likely that there are several exciting sources, as bolstered by recent mid-infrared imaging of the region (Smith et al. 2004).

As the nearest regions of ongoing massive star formation, these density peaks in OMC-1 are clear targets for detailed study at all wavelengths. The most recent detailed X-ray study of OMC-1 is that of Garmire et al. (2000), who observed the region using *Chandra* and ACIS-I with an exposure time of 47.8 ks (0.6 days). In BN-KL, the luminous infrared Source n was seen, which may constitute the first unambiguous (i.e. spatially resolved from other young stars) X-ray detection of a massive YSO. Faint X-ray emission was also seen close to, but apparently not coincident with BN, and it remained unclear whether or not the emission was coming from a separate, nearby source, or was being produced in the outflow from BN (Garmire et al. 2000; Tan 2004).

In January 2003, *Chandra* and ACIS-I were again used to observe the region, but this time for a total of 838 ksecs (~ 10 days), yielding an exceptionally deep study known as the *Chandra* Orion Ultradeep Project or COUP (see Getman et al. 2005b). Here we concentrate on the X-ray sources detected along the line-of-sight towards BN-KL and OMC-1S with the following main goals: to complete the census of obscured YSOs in these regions as traced through their X-ray emission; to investigate the nature of the X-ray sources associated with luminous mid-infrared stars in the BN-KL region; and to study the X-ray luminosity function of obscured sources in OMC-1.

After briefly reviewing the observations and data analysis in §2, we present an overview of the X-ray sources and their counterparts in BN-KL in §3, before discussing X-ray emission from BN and the rotational modulation of the X-ray source close to BN in §3.1, and then examining other X-ray sources close to luminous mid-infrared stars in BN-KL in §3.2. The X-ray sources and their counterparts in OMC-1S are reported in §4, before a broader view is taken of the disk fraction in OMC-1 in §5 and of the embedded stellar population of OMC-1 in §6. Our conclusions are presented in §7.

2. Observations and data analysis

COUP combines six near-consecutive exposures at a single pointing ($05^h\,35^m\,17.0^s$, $-05^\circ\,23'\,40.0''$, J2000) over 13.2 days in January 2003, yielding a total on-source exposure time of 838 ks (9.7 days). The observations were obtained using ACIS-I (Garmire et al. 2003) on-board the *Chandra* X-ray Observatory (Weisskopf et al. 2002). Getman et al. (2005b) present a detailed discussion of the COUP data, encompassing source detection, photon extraction, spectral analysis, and variability analysis. Here, we focus a subsample of the 1616 COUP source catalog and data products of Getman et al. (2005b), limited to X-ray sources along the line-of-sight towards two key regions of the OMC-1 molecular cloud, namely BN-KL and OMC-1S, both located at about 1.2′ off-axis in the COUP pointing.

Figure 1 shows a 450 μm wavelength image of the part of OMC-1 behind the core of the ONC (Johnstone & Bally 1999), where the two main submillimetre peaks delineate the BN-KL and OMC-1S regions: COUP sources are plotted for comparison. Lightly obscured COUP sources ($N_{\rm H} < 10^{22}\,{\rm cm}^{-2}$) are seen to be clustered around the Trapezium OB stars and can be classified as ONC members. By contrast, we can analyse the spatial distribution of the more obscured ($N_{\rm H} \geq 10^{22}\,{\rm cm}^{-2}$) COUP sources. Their surface density is calculated using the kernel method and adopting a Gaussian shape kernel (Gomez et al. 1993, and references therein), with a smoothing length[1] of 11.5″, i.e. 0.025 pc at 450 pc. The obscured X-ray sources are seen to concentrate in three clusters associated with BN-KL, OMC-1S, and the Trapezium OB stars, with peak surface densities of 3800, 2800, and 2900 sources pc^{-2}, respectively. Lada et al. (2004) found a similar result by selecting all sources with infrared $K-L$ colors greater than 1.5 mag, roughly corresponding to $A_{\rm V} > 15$–26 mag.

In order to proceed further with our analysis, we adopt semi-arbitrary definitions of BN-KL as the region shown in Fig. 6 of Garmire et al. (2000), i.e. a $40'' \times 50''$ area centered on BN, and for OMC-1S, a $60'' \times 75''$ area centered roughly on the corresponding submillimetre peak, covering the clustering of obscured X-ray sources.

Figure 2 shows a full resolution ($0.492'' \times 0.492''$ pixel) view of our BN-KL region in the 0.5–8 keV band. Colors represent the photon energy where red, green, and blue show soft unabsorbed (0.5–1.7 keV), medium (1.7–2.8 keV), and hard (2.8–8.0 keV) energy photons, respectively. This composite image was produced using the algorithm recently proposed by Lupton et al. (2004), which ensures that a given X-ray photon color is mapped to a unique color in the RGB image, and

[1]The kernel density estimator is defined at each point (α, δ) of the computation grid by: $D(\alpha,\delta) = \frac{1}{h^2}\Sigma_{i=1}^{n} K(\alpha_i, \delta_i, \alpha, \delta)$, where h is the smoothing length, (α_i, δ_i) are the positions of the n sources, and K is the weight function. Here we adopt a Gaussian shape for the kernel: $K(\alpha_i, \delta_i, \alpha, \delta) = \frac{1}{2\pi}\exp(-r^2/2h^2)$, where $r^2 = (\alpha - \alpha_i)^2 \cos^2\delta_i + (\delta - \delta_i)^2$.

that the color is correct even when the intensity is clipped at unity, compared to the burnt-out white produced by the standard RGB method. The 43 X-ray sources detected by COUP in this region above a limit of 3 net photons are plotted. Figure 3 shows the equivalent COUP 0.5–8 keV color composite image of the selected OMC-1S region, along with the positions of the 60 X-ray sources detected above the 3 net photons limit.

Table 1 and Table 3 list the X-ray sources seen along the line-of-sight towards BN-KL and OMC-1S, respectively, with their basic X-ray properties as adapted from Getman et al. (2005b). Also given are associations with previously catalogued sources at optical, near- and mid-infrared wavelengths, along with other identifications with, for example, radio sources. Of note in this latter regard are the spatial offsets between the COUP source and the nearest near-infrared source from the unified VLT JHK_S catalog of McCaughrean et al. (2005, in preparation): the RMS offset between the X-ray and near-infrared sources is only 0.2″, demonstrating the certainty to which such associations can be made. Finally, an indication is given of the membership status of each X-ray source with respect to the region, as determined by Getman et al. (2005a). Comments on individual COUP sources are given in Appendix A.

The X-ray properties of the BN-KL and OMC-1S X-ray sources are described in more detail in Table 2 and Table 4, respectively (adapted from Getman et al. 2005b). These include measures of the hardness ratio, column density, plasma temperatures, emission measures, observed and extinction corrected luminosities, and an assessment of the source variability.

3. X-ray sources along the line-of-sight towards BN-KL

Despite a total exposure time some 17.5 times longer than that of Garmire et al. (2000), COUP revealed just 17 new X-ray sources along the line-of-sight towards the BN-KL field, an increase of just 65%. As discussed in §6, this is due to a combination of factors, including the underlying stellar mass function in the region and the correlation between L_X and L_{bol}, which is roughly linear in the stellar regime (see Figs. 1–5 of Preibisch et al. 2005a) and possibly steeper in the brown dwarf regime (see Fig. 5 of Preibisch et al. 2005b).

The left panel of Fig. 4 shows the distribution of column densities for sources seen along the line-of-sight towards the region we have selected centered on BN-KL. A bimodal distribution is clearly seen. Half of the X-ray sources have optical counterparts: we find 21 X-ray emitting optical stars compared to the 14 detected previously. The distribution shows that these sources have a median extinction of $\sim 4\times10^{21}$ cm^{-2}, i.e. $A_V \sim 2.5$ mag only, and it seems entirely likely that these unobscured sources are members of the foreground ONC population centered on the Trapezium OB stars, just 0.1 pc away. Conversely, the second peak in the column density distribution are

obscured by median column density of $\sim 10^{23}$ cm^{-2}, i.e. $A_V \sim 70$ mag; these sources are embedded in the background OMC-1 molecular cloud and while none have optical counterparts, all but five do have infrared stellar counterparts.

One concern is that some of the heavily embedded sources with or without infrared counterparts may be background AGNs seen in X-rays through the cloud. Getman et al. (2005a) have investigated the anticipated level of such contamination in the COUP sample by making Monte-Carlo simulations of COUP detected extragalactic background sources, using the expected $\log N$–$\log S$ for X-ray background AGNs (Giacconi et al. 2001) convolved with the optical depth map for the OMC (derived from ^{13}CO map of Bally et al. 1987), and the COUP background map. Getman et al. (2005a) estimate that ≤ 1 background AGNs should be seen towards our BN-KL region, since the considerable extinction associated with the OMC shields us from such contamination.

In qualitative support of this finding, we see that the most deeply embedded X-ray sources in the BN-KL region, i.e. those without near-infrared counterparts, all display time variability characteristic of young low-mass stars with X-ray flares (see Fig. 5). The same is true of many other X-ray sources in the region: Fig. 6 shows the most variable X-ray source in the region, the obscured COUP 580 ($\log N_H \simeq 22.2$, i.e. $A_V \sim 10$ mag), which displayed a remarkable series of six impulsive X-ray flares.

3.1. X-rays from BN and its vicinity

It has long been unclear whether BN is an X-ray emitter. Although there is considerable X-ray emission from the vicinity, earlier X-ray surveys with *Einstein* (Ku & Chanan 1979) and *ROSAT/HRI* (Gagné et al. 1995), for example, did not have sufficient spatial resolution and sensitivity to hard X-rays, respectively, to know whether any of this X-ray emission came from BN itself.

In the first 1999 *Chandra* observations of Garmire et al. (2000), a source with just 18 photons was seen very close to BN, but with a measured positional offset of 1.1″, too far from BN to be considered as a true coincidence. The analysis of the combined 1999–2000 data by Feigelson et al. (2002) found a total of 42 photons, no variability, a very hard spectrum with plasma energy > 10 keV and absorption $\log N_H \simeq 22.6$, and a hard band X-ray luminosity of $\log L_h \simeq 29.4$. They found a positional offset of 0.6″ from the infrared source which, they stated in a footnote, was consistent with a true coincidence.

More recently, Tan (2004) showed that the X-ray emission lies roughly north-west of BN, along the projected proper motion vector of this rapidly moving source. As a consequence, Tan (2004) proposed that the X-ray emission does not come from BN itself, but rather from bowshock

preceding the source in its passage through OMC-1. With the substantially deeper COUP data, we are in a better position to assess this suggestion and reanalyse the question of whether or not the X-ray emission is indeed coincident with the near-infrared source.

3.1.1. COUP 599a: An X-ray bright companion to BN

In the COUP data, the nearest source to the nominal near-infrared position of BN as listed in the unified VLT catalog of McCaughrean et al. (2005, in preparation) is COUP 599a, which shows a total of 847 counts which can be successfully modeled by an isothermal plasma with $kT = 2.6\,\mathrm{keV}$, a column density of $\log N_\mathrm{H} = 23.0$ (Fig. 7), a luminosity of $\log L_\mathrm{h} = 30.2$ after correction for absorption, and variability over the 13 days of COUP observations by a factor of five in amplitude (see Fig. 7 and §3.1.3).

But is COUP 599a in fact BN? Attempting to answer this question definitively, we have carried out a careful astrometric check. For overall consistency, the astrometry in the VLT catalog was derived from the K_S band mosaic image of the region. However, BN is heavily saturated at $K_\mathrm{S} \sim 5\,\mathrm{mag}$ and due to the peculiar way in which infrared arrays saturate, its pixel position in that mosaic had to be defined by eye rather than via a centroid.

Given the present detailed interest in BN, we can do a better job using the VLT J_S band data, in which BN is much fainter ($\sim 15\,\mathrm{mag}$) but still readily visible with high signal-to-noise, making an accurate determination possible. We took a single, non-mosaiced J_S band image covering BN from January 2002, one year prior to the COUP exposure. In this image, we established a local reference frame based on $\sim$10–15 nearby sources which are unsaturated in both the J_S and K_S data, and for which accurate sky coordinates are available from the VLT catalog, where the overall astrometric error with respect to the 2MASS (FK5) reference frame is 0.15″ RMS (McCaughrean et al. 2005, in preparation).

Doing so, we obtained an epoch 2002.0 position for BN of $05^\mathrm{h}35^\mathrm{m}14.130^\mathrm{s}$, $-05^\circ22'22.72''$ (J2000.0), with an astrometric error with respect to the local reference frame of 0.084″ RMS. In order to make a consistency check, we also repeated the same process for J_S VLT frames covering BN from December 1999 and January 2001, spanning the full length of the VLT project. We find essentially the same positions for BN in both years as for January 2002, giving us confidence in the accuracy of the position in the 2MASS global frame.

We have also pushed the VLT data a little further and searched for evidence of the proper motion in BN with respect to the surrounding stars in a local x, y pixel coordinate reference frame (as opposed to the global α, δ frame), under the assumption that these sources are relatively fixed over a two year period (the ONC 2D velocity dispersion of $\sim 3.3\,\mathrm{km\,s^{-1}}$ corresponds to 1.5 millarcsec

per year at Orion). We do see a slight shift in BN from year to year, on the order of 0.01–0.03″ to the NW, although the fit errors are on the same order and thus the result is marginal at best.

Therefore, we have simply taken the VLT-determined position from January 2002 and applied the radio-derived proper motion for BN of $0.0181 \pm 0.0022''$ yr^{-1} at position angle $-37.7 \pm 5°$ (Tan 2004) to yield a projected epoch 2003.04 (i.e. at the time of the COUP observation) position for BN of $05^{h}35^{m}14.129^{s}$, $-05°22'22.71''$ (J2000.0).

This position lies 0.895″ (~ 400 AU) south-east of COUP 599a. The RMS astrometric error between the COUP and VLT frames is 0.25″ (Getman et al. 2005b) and locally the alignment is often better: no other source in the vicinity of BN has an X-ray/infrared offset larger than 0.25″. Thus, we can conclude with confidence that COUP 599a is not BN.

What is COUP 599a then? Tan (2004) proposed that the X-ray emission seen just to the northwest of BN, i.e. COUP 599a, originated in a wind bow shock as BN moves rapidly through OMC-1. However, we now see that COUP 599a has strong, rapid variations in its flux and spectrum, and such variability is incompatible with the relatively constant X-ray emission that would be produced by such a shock. In fact, these properties make it much more likely that COUP 599a is simply a deeply embedded lower-mass source in OMC-1, plausibly a companion to BN with a ~ 400 AU separation, or otherwise just an unrelated cluster member along the same line-of-sight.

The column density $\log N_{\rm H} = 23.0$ inferred from the X-ray spectrum of COUP 599a corresponds to an extinction of $A_{\rm V} \sim 50$ mag, or ~ 14 mag in the $J_{\rm S}$ band. Since there no source detected at the position of COUP 599a in the VLT $J_{\rm S}$ band data to a limiting magnitude of ~ 21 mag, COUP 599a must have an intrinsic magnitude fainter than $J_{\rm S} \geq 7$ mag at Orion, or an absolute magnitude of $M_{J_{\rm S}} \geq -1.3$. From the 1 Myr isochrone of Siess et al. (2000), this corresponds to an upper limit mass of $\geq 4\,M_{\odot}$, i.e. COUP 599a could be a relatively massive star. In principle, stricter upper limits could be set on the mass of COUP 599a by using the VLT H and $K_{\rm S}$ band data, but since BN is already quite bright by 1.5 μm and less than 1″ away, the VLT data are saturated at the location of COUP 599a and thus it is impossible to claim any meaningful limits on its non-detection at the longer wavelengths. In any case, it seems quite plausible that COUP 599a is a deeply embedded lower-mass star, either unrelated or a companion to BN. Companions to higher-mass stars are commonly found to be more X-ray luminous than the massive primary, both in field and in unabsorbed ONC intermediate-mass stars (Stelzer et al. 2003, 2005).

3.1.2. COUP 599b: A second companion or BN itself?

Having established that COUP 599a is not BN, the question remains whether or not any fainter X-ray emission has been detected from BN itself in the extremely deep COUP exposure. In order

to pursue this question further, we used the IDL Astrolib `MAX_LIKELIHOOD` routine to carry out an image deconvolution over a $43'' \times 47''$ region around BN. The routine iteratively seeks the Maximum Likelihood (ML) restoration of a blurred image with additive Poisson noise (Richardson 1972; Lucy 1974). The input point spread function was that obtained from the *Chandra* simulation program `MARX` assuming the appropriate spectral parameters for COUP 599a and the deconvolution was stopped after 500 iterations.

All but one of the new features revealed in the reconstructed image are consistent with noise unrelated to any known source at other wavelengths. The exception is a faint point source, COUP 599b, which lies $\sim 0.82''$ southeast of COUP 599a. Figure 8 shows a small portion of the original COUP image, the corresponding ML reconstruction and a closeup of a $\pm 1.5''$ region around BN.

COUP 599b lies $0.4''$ from the VLT position for BN: as described above, this is a significantly larger offset than seen between VLT and COUP associations in the immediate vicinity. Similar offsets (0.3–$0.4''$) are seen between COUP 599b and the VLA radio positions for BN as given by Menten & Reid (1995), Tan (2004), and Zapata et al. (2004a). We found that the Menten & Reid (1995) radio positions for Source n and Source I matched those for Sources 17 and 19 of Zapata et al. (2004a), and that then slight adjustments ($\Delta\alpha = -0.080''$ and $\Delta\delta = +0.038''$) were necessary to bring the Zapata et al. (2004a) frame into alignment with the COUP/VLT frame. After doing so, the Zapata et al. (2004a) position for BN was also $0.4''$ from COUP 599b.

Thus it appears as though COUP 599b is not BN either. However, COUP 599b was detected with only $\simeq$ 50–70 photons in the PSF wings of COUP 599a and it is difficult to assess the positional errors after the iterative ML deconvolution, and thus we cannot completely exclude the possibility that COUP 599b coincides with BN: further work will be needed. For reference, a qualitative examination of likely COUP 599b photons suggests a heavily absorbed source with a low-energy cutoff similar to that seen in COUP 599a ($\log N_{\rm H} = 23.0$), an estimated luminosity of $L_{\rm h} \sim 10^{29}$ erg s^{-1}, and no dramatic variability during the 13-day COUP observation.

Both possibilities are consistent with the COUP results concerning B stars in the unobscured Orion Nebula Cluster (Stelzer et al. 2005). Some of these show X-rays coincident with the massive component, which may arise from the massive star or from an unresolved close binary, while others are resolved from the massive star as wide-binary companions. The case of θ^1 Ori B is particularly instructive. It is known from infrared imaging to be at least a quintet and has two associated COUP sources separated by $0.9''$. It is not possible to unambigously assign the X-rays to the components of this hierarchical system, but one X-ray component has a softer spectrum and slow, low-amplitude variability which may arise from the B2.5 primary, while the other has a hard spectrum and high-amplitude flaring likely associated with a binary low-mass subsystem.

3.1.3. Periodic X-ray modulation of COUP 599a

During a month-long (March–April 2000) near-infrared monitoring campaign, Hillenbrand et al. (2001) found a puzzling nearly sinusoidal periodic variability in BN in the H and K_S bands. The period was 8.28 days and the peak-to-peak amplitude was ~ 0.2 mag, as measured in a $4''$ radius aperture, i.e. nominally covering both COUP 599a and COUP 599b.

Although our astrometric study suggests quite strongly that neither of these two X-ray sources is in fact BN, we have nevertheless made a detailed study of variability in the X-ray emission from COUP 599a, as there are sufficient photons to do so. There are several potential sources of variability in main-sequence and pre main-sequence stars: flares, the evolution of active regions, time-variable mass accretion (Flaccomio et al. 1999), modulation due to the inhomogeneity of the emitting region combined with stellar rotation, and so on.

Thanks to the 13 day length of the COUP observation, we are able to search for variability on similar timescales or less. The discovery of rotational modulation would be of particular interest as it would reveal the degree of inhomogeneity of the X-ray emitting plasma at the stellar surface. For our analysis of COUP 599a, we closely followed the methods used by Flaccomio et al. (2005) for their extensive study of rotational modulation in the COUP sample. In brief, we computed the Lomb-Scargle Normalized Periodogram (hereafter LNP; Lomb 1976; Scargle 1982) on the binned light curve. Peaks in the LNP were identified and False Alarm Probabilities (FAP) computed for each of them using Monte Carlo techniques assuming correlated noise. The correlation timescale employed was on the order of the length of flares seen in COUP 599a as described below.

Figure 9 shows the light curve for COUP 599a. There is an underlying gradual variability, with the suggestion of periodicity: there is also a flare lasting ~0.5 days 2003 January 12 which was detected using the algorithm described by Wolk et al. (2005). We have performed the LNP analysis on the whole light curve minus this flare and a short time afterwards, as indicated in Fig. 9 by a horizontal bar, while Fig. 10a shows the corresponding periodogram. The largest peak appears at a frequency of 0.121 days^{-1}, corresponding to a period $P_{\rm rot,X} = 8.27 \pm 0.10$ days.

Dashed lines in the figure indicate LNP power thresholds of 1% and 0.1%, computed using 10000 Monte Carlo simulations and assuming a correlation time-scale, τ_{corr}, of 15 hrs. The simulations show that the 8.27 day peak has an FAP of $\sim 0.1\%$, while changing τ_{corr} across the range 5–25 hrs yields an FAP from $< 0.01\%$ to 2%. Figure 10b shows the COUP 599a light curve folded with the 8.27 day period and repeated twice to show the periodicity more clearly. Different symbols indicate time bins belonging to different rotation cycles. We have also repeated the LNP analysis on the whole light curve, i.e. retaining the flare on 2003 January 12, which yields a similar period ($P_{\rm rot,X}$=8.08 days) but with a somewhat lower significance (FAP = 0.4%).

The apparent ~8.3 days X-ray periodicity in COUP 599a is so similar to the infrared period

measured by Hillenbrand et al. (2001) for BN that, at first sight, it seems it cannot be coincidental. However, it is extremely hard to understand this result, given that the X-ray variability is associated with a source that is offset by $\sim 0.9''$ the infrared-variable BN. First, even though COUP 599a lies within the aperture monitored by Hillenbrand et al. (2001), there is no evidence for an infrared source there at the magnitudes that would be necessary to induce an apparent variability in BN. Imagine that BN is in fact constant at $H = 9.2$ mag, but that it appears to be variable by 0.2 mag in a large aperture due to the proximity of another source which *is* varying. The most extreme situation would be if the adjacent source is varying by 100 %, in which case, in its full-on state it would be adding 0.2 mag to the brightness of BN, i.e. it would have a magnitude of $H = 10.9$ mag in this state. It is straightforward to show that in all other scenarios, in which the adjacent star varies by less than 100%, it would need to be brighter than $H = 10.9$ mag in its full-on state, and the VLT images emphatically rule out the presence of a source with anything like that brightness within $1''$ of BN.

The next explanation would be that both BN and the COUP 599a exhibit near identical ~ 8 day periodicities because they are physically linked, but this seems equally unpalatable, as we cannot imagine a physical effect able to link the rotations, orbits, or magnetic activities of stars separated by > 400 AU.

The third option is that the X-ray variations of COUP 599a do not in fact represent a true periodicity, despite the apparent statistical significance of the periodogram peak. Such features can arise in time series from aperiodic autoregressive (i.e. $1/f$-type noise) processes. The non-sinusoidal shape of the folded lightcurve (Fig. 10b) supports the idea that the variations are non-rotational in origin and thus possibly aperiodic. In this case, the apparent similarity of the near-infrared and X-ray variations would arise purely by chance and with no astrophysical meaning.

3.2. Other X-ray sources close to luminous mid-infrared stars in BN-KL

BN is not the only luminous source in the BN-KL region: Sources I (Churchwell et al. 1987) and L (Menten & Reid 1995) are radio continuum sources associated with compact H II regions, where radio Source L is also coincident with the luminous infrared Source n (Lonsdale et al. 1982).

COUP detected no X-ray emission from radio Source I. On the other hand, radio Source L (infrared Source n) has been previously detected by *Chandra*, both by Garmire et al. (2000, their source 13) at a level of 61 counts using ACIS-I and by Flaccomio et al. (2003, their source 272) using the HRC-I, at a level $\gtrsim 3$ times than that measured by the first ACIS-I observation. Our longer *Chandra* exposure detected a total of 3779 counts from COUP 621, coincident with Source n, which makes a more detailed study of its X-ray properties possible. Figure 11 shows the light

curve of COUP 621, displaying several impulsive X-ray flares typical of the activity of low-mass stars. The suggestion then is that COUP 621 is a lower-mass companion to the luminous and higher-mass Source n.

In passing, it must be noted that COUP 621 is not coincident with the possible low-mass companion to Source n recently detected 0.6″ to its northwest using the infrared adaptive optics system NACO on the VLT (Lagrange et al. 2004). Indeed, the $\log L_{\rm h,c} = 30.7$ determined for COUP 621 implies a relatively high mass, ~ 1–$3\,M_{\odot}$ (Wolk et al. 2005; Preibisch et al. 2005a), but is also consistent with intermediate-mass B star multiple systems (Stelzer et al. 2005).

Finally, X-ray emission is also seen associated with two other luminous mid-infrared sources in BN-KL: COUP 628 and COUP 589 are X-ray counterparts to component C of IRc2 and component i2 of IRc3 (Dougados et al. 1993), respectively. Figure 11 shows the corresponding X-ray light curves. A plausible interpretation is that we are again seeing lower-mass components of the higher-mass multiple systems IRc2 and IRc3.

4. X-ray sources along the line-of-sight towards OMC-1S

As with BN-KL, the number of new sources (31) detected in the OMC-1S region is relatively small, despite the 17.5 times longer exposure of COUP relative to the original ACIS-I observations of Garmire et al. (2000), and also as with BN-KL, the most likely explanation lies in the shape of the X-ray luminosity function (see §6).

One-third of the COUP sources within the region we have defined as OMC-1S have optical counterparts. The right panel of Fig. 4 shows the distribution of column densities for these sources, with a median value of $\sim 2.3 \times 10^{21}\,{\rm cm}^{-2}$, i.e. $A_{\rm V} \sim 1.5\,{\rm mag}$. These relatively unobscured sources are thus likely associated with ONC, since OMC-1S lies within 1′ in projection from the centre of the cluster. The other COUP sources along the line-of-sight towards OMC-1S are obscured by a median column density of $\sim 1.6 \times 10^{23}\,{\rm cm}^{-2}$ or $A_{\rm V} \sim 100\,{\rm mag}$ (Fig. 4); all but 18 of these sources have near-infrared stellar counterparts.

By design, the VLT $JHK_{\rm S}$ catalog of McCaughrean et al. (2005, in preparation) lists only point sources, but the VLT images show a number of extended nebula sources which also exhibit X-ray emission (see also Kastner et al. 2005). Of particular note in OMC-1S is COUP 554, which is seen in the near-infrared as a red nebulosity with a FWHM of $\sim 1.5''$ or ~ 700 AU, with a somewhat more extended low-level extension to the southwest. It appears to be a small reflection nebula at the opening of a cavity surrounding a deeply embedded YSO and has long been implicated as signposting one of the key embedded sources in the OMC-1S region (source S1 of McCaughrean 1988).

The X-ray emission from COUP 554 is characteristic of a T Tauri star: its light curve and spectrum are shown in Fig. 12. It is slightly displaced to the northeast with respect to the centroid of the near-infrared emission, supporting the embedded YSO and reflection nebula scenario. COUP 554 is also detected at mid-infrared wavelengths (IRS4 of Smith et al. 2004) and at 1.3 cm (source 136-356 of Zapata et al. 2004b), but not at 3.6 cm, again supporting the presence of an embedded YSO.

Finally, according to Gaume et al. (1998, component B) this source displays no near-infrared excess, whereas Lada et al. (2000, source TPSC-46) claim that there is evidence for near-infrared excess, but given that the source is now clearly seen to be extended at those wavelengths, it is not immediately obvious that this can be directly related to the presence of a disk or protostellar status.

Just to the south of COUP 554, COUP 555 is also associated with a mid-infrared source (Smith et al. 2004, IRS5) and 1.3 cm radio emission (Zapata et al. 2004b, source 136-359), but this time also with a near-infrared point source (Gaume et al. 1998, component C; VLT catalog source 382). It also has the characteristics expected of an embedded T Tauri star, rather than a protostar as suggested by Lada et al. (2000, source TPSC-16).

Few if any of the X-ray sources without near-infrared counterparts are expected to be background AGN shining through the cloud, as was also the case for BN-KL. The Getman et al. (2005a) modelling of possible background extragalactic contaminants predicts that only ~ 1 AGN should be seen over the OMC-1S area. Thus most of the remaining 18 X-ray sources without near-infrared counterparts are expected to be genuine embedded YSOs. Figure 13 shows their X-ray light curves: several X-ray flares are evident. Seven of these sources (namely COUP 582, 594, 615, 633, 641, 659, and 667) are seen to lie in a small region just to the southeast of the core of OMC-1S and likely represent a new subcluster of embedded YSOs. One of these sources, COUP 594, was recently detected in a sensitive VLA 1.3 cm observation of the region where it displayed a large ($\sim 20\%$) right circular polarization indicative of gyrosynchrotron emission from the active magnetosphere of a young low-mass star (source 140-410 of Zapata et al. 2004b).

Conversely, it is worth looking at the most luminous mid- and far-infrared sources in OMC-1S and examining their X-ray properties. No X-ray emission was detected at the position of the luminous far-infrared/sub-millimetre source FIR4 (Mezger et al. 1990) or at the dense molecular condensation CS3 (Mundy et al. 1986), both of which were suggested to be the the exciting source of an embedded, highly collimated molecular outflow (Schmid-Burgk et al. 1990). Similarly, COUP did not detect the brightest mid-infrared source in OMC-1S, IRS1 of Smith et al. (2004), located at the base of the prominent jet that powers HH 202, or IRS3 of (Smith et al. 2004), the third most luminous mid-infrared source in the region. Lastly, no X-ray emission was detected at the exact location of 'Optical Outflow Source' of O'Dell & Doi (2003) (see Fig. 3).

The nearest X-ray source to the OOS is COUP 632, 3.8″ away from it. COUP 632 is a faint source with just 16 counts collected, but is remarkably the most embedded X-ray source in the entire COUP catalog, with $\log N_{\rm H}$=23.94, i.e. $A_{\rm V} \sim 500$ mag (see Fig. 14 for its light curve and X-ray spectrum). This extreme level of extinction could be produced by a circumstellar envelope plus a disk seen close to edge-on, and indeed, COUP 632 is associated with the second brightest mid-infrared source in the region, IRS2 of Smith et al. (2004). The spectral energy distribution of IRS2 continues to rise to 20 μm indicating a large infrared excess typical of a Class I source, i.e. an evolved protostar (see Fig. 1 of Smith et al. 2004). It was also suggested to be a protostellar candidate by Lada et al. (2000, source TPSC-1).

Smith et al. (2004) proposed that COUP 632/IRS2 was the most likely driving source of the HH 529 jet which extends east from OMC-1S at a position angle of $\sim 100°$; O'Dell & Doi (2003) had previously linked HH 529 with their OOS. The source was also recently detected at 1.3 cm (source 144-351 of Zapata et al. 2004b), but not at 3.6 cm (Zapata et al. 2004a), and as its bolometric luminosity ($\gtrsim 7.9\,L_\odot$; Smith et al. 2004) is too small to drive an H II region, Zapata et al. (2004a) proposed that the radio emission emanates from the magnetosphere (gyrosynchrotron emission) or the ionized outflow (free-free emission) of a low-mass star.

5. Near-infrared disk emission from X-ray sources in OMC-1

Approximately 70% of the X-ray detected stars in BN-KL and OMC-1S have near-infrared counterparts and we have examined these sources in near-infrared color-color diagrams (see Fig. 15) to explore the fraction with excess emission due to disks (e.g., McCaughrean et al. 1996; Hillenbrand et al. 1998; Lada et al. 2000, 2004). A given source is said to have a excess emission if it lies to the right of the main sequence colors with extended reddening vectors, after allowing for 0.1 mag photometric errors in all three bands used in a given color-color diagram.

We have used three different color-color diagrams, namely $H - K_{\rm S}$ vs. $J - H$, $K_{\rm S} - L'$ vs. $J - H$, and $K_{\rm S} - L'$ vs. $H - K_{\rm S}$, combining the VLT data of McCaughrean et al. (2005, in preparation) with the L' data of Lada et al. (2004). There appears to be little difference between BN-KL and OMC-1S, with the latter perhaps including a handful more extremely red sources than the former, suggesting that OMC-1S may be younger and its YSOs more deeply embedded. However, BN-KL is a much more confused region than OMC-1S given the brightness of BN itself and the surrounding nebulosity, and thus faint, extremely red sources will be harder to see there.

In both BN-KL and OMC-1S, the excess fraction increases from $\sim 25\%$ in the first diagram to $\sim 60\%$ in the last, similar to the results obtained by Lada et al. (2004) for stars in the core of the ONC without any selection on X-ray properties. Under the assumption that excess emission is

due to circumstellar disks, we therefore deduce that these deeply embedded star formation sites in OMC-1 have disk fractions indistinguishable from the larger cluster.

6. Stellar population of OMC-1

Having examined the two regions and individual sources within them in detail, we can now look at the overall properties of the populations of X-ray sources embedded in BN-KL and OMC-1S. In order to differentiate between embedded OMC-1 sources and unobscured foreground ONC stars along the line-of-sight to the two regions, we consider only X-ray sources without optical counterparts and with $\log N_{\rm H} \geq 22$ (see Fig. 4). As we continue, recall that BN-KL, with its $\sim 10^5\,{\rm L}_\odot$ (Werner et al. 1976; Genzel & Stutzki 1989, and references therein) has ten times the luminosity of OMC-1S.

6.1. X-ray luminosity function comparisons

Different young stellar clusters, including the ONC, NGC 1333, and IC 348, appear to have X-ray luminosity functions (XLFs) with a universal lognormal shape (Feigelson & Getman 2005). Once a richness-dependent tail above $\log L_{\rm t} \leq 31.5$ is removed, the XLF appears lognormal with a mean $< \log L_{\rm t} >= 29.3$ and standard deviation $\sigma(\log L_{\rm t}) = 1.0$ (Feigelson et al. 2005). The shape of the XLF can be roughly understood as a convolution of the IMF, which breaks from the Salpeter powerlaw below $\simeq 0.5\,{\rm M}_\odot$, and the correlation between X-ray luminosity and mass. These two effects result in a steep fall-off in the number of fainter X-ray stars in a young stellar cluster, explaining why the factor of ten increase in the limiting sensitivity of COUP over previous *Chandra* observations of the region led to only a very small increase in the number of detected lightly-absorbed ONC stars. If we assume that the stellar populations embedded in the OMC-1 cores have a similar average XLF shape, then we can infer the total obscured population from a comparison of the incomplete (due to obscuration) OMC-1 source counts with the more complete ONC source counts. We restrict our analysis to the hard X-ray band as that is less affected by obscuration.

Following Preibisch et al. (2005a), our ONC reference counts are taken from the COUP 'lightly absorbed optical sample', which comprises sources from Hillenbrand (1997) which were classified as ONC members, for which spectral types are known, and which have $A_{\rm V} \leq 5\,{\rm mag}$.

The lightly absorbed optical sample consists of 584 stars, 551 of which were detected as X-ray sources by COUP and have X-ray hard band corrected luminosities. For the 33 stars in the lightly absorbed optical sample which were not detected by *Chandra*, we used PIMMS to

transform the count rate upper limits into the luminosity upper limits, assuming a Raymond-Smith plasma spectrum with a temperature of $kT = 1$ keV, 0.2 times solar abundance, and computing the absorbing hydrogen column from the visual extinction, according to the relation $N_{\rm H} = A_{\rm V} \times 1.6\,10^{21}\,{\rm cm}^{-2}\,{\rm mag}^{-1}$ (Vuong et al. 2003).

Table 5 summarizes the statistics of the BN-KL and OMC-1S samples. The obscured samples of BN-KL and OMC-1S consist of 22 and 36 stars, respectively, but hard band luminosities are available for only 21 and 32 stars.

Figure 16 shows histograms of the differential XLFs in the unobscured ONC, and in the obscured samples of BN-KL, and OMC-1S. The observed (absorbed) hard band luminosities are in panels (a)–(c), while the intrinsic (corrected for absorption) hard band luminosities in panels (d)–(f). Quantitative analysis is more readily performed using the integral XLFs in Fig. 17, where ONC XLF is the maximum-likelihood Kaplan-Meier estimator[2]. We can see that the OMC-1 stellar populations have average luminosities systematically higher by $\Delta\log L_{\rm h,c} \sim 1$ than the unobscured ONC population. This difference is present at a significance level of P=99.48–99.98%. On the other hand, the BN-KL and OMC-1S XLFs are statistically indistinguishable.

The elevated XLFs of the OMC-1 obscured populations is consistent with the reasonable presumption that more heavily absorbed fainter stars are missing from the samples. We therefore introduce into the OMC-1 samples a distribution of missing stars mimicking the distribution of unobscured ONC stars in the interval $26.5 \le \log L_{\rm h,c} \le 29.5$ (i.e. from the minimum $\log L_{\rm h,c}$ of the ONC sample to about 80% of the XLF of the OMC-1 samples). Forty trial sets were computed for each trial number of added stars. In order to make the XLFs compatible with that of the unobscured ONC sample at the P=10 % confidence level, 13 and 10 stars had to be added to the 21 and 32 stars with measured $L_{\rm h,c}$ of BN-KL and OMC-1S, respectively. There are 1 and 4 faint X-ray sources in BN-KL and OMC-1S, respectively, which have no hard X-ray luminosities and were therefore not included in our XLF analysis, leaving 18 of the 23 nominally 'missing' X-ray stars in OMC-still to be identified.

Twenty-five stars had to be added to each region to bring their mean and median XLF values to the same levels as the unobscured ONC sample. If >50 stars were added to each region, their XLFs become too heavily weighted at low luminosities at the $P < 10\%$ confidence level. From this analysis, we estimate that the true populations of obscured sources in BN-KL and OMC-1S are ≃46 and 57 stars, with 90% confidence intervals of 34–71 and 42–82 stars, respectively.

---

[2]This estimator of the empirical distribution function takes into account the nondetections in ONC sample. The Kaplan-Meier and two-sample statistical methods used here – the Gehan and Peto-Peto generalized Wilcoxon tests and the Logrank test – are standard methods of univariate survival analysis as described by Feigelson & Nelson (1985).

6.2. Initial Mass Function comparisons

We now extend this analysis to an examination of the stellar initial mass function (IMF) for obscured X-ray sources in BN-KL and OMC-1S. The procedure developed here is approximate and its reliability is uncertain. For example, we do not account for scatter or nonlinearity in the ONC X-ray/mass relation based on the evolutionary tracks of Siess et al. (2000), nor for the inefficiency of COUP in detecting the very-low-mass population of any Orion sample. Nonetheless, this effort gives the first estimate of the full IMF associated with the OMC-1 cores. Previous studies of these populations were limited to luminous OB stars or protostars with heavy disks and/or jets.

Starting with the observed $\log L_{\rm h,c}$ sample, a correction to $L_{\rm h,c}$ values is applied to convert it to total X-ray luminosity in the 0.5–8 keV energy corrected from absorption, $L_{\rm t,c}$. From the ONC optical sample, excluding stars with $T_{\rm eff} > 6000$ K, we obtain $\log L_{\rm t,c} = 0.81(\pm0.01) \times \log L_{\rm h,c} + 6.1(\pm0.3)$. We then apply the X-ray luminosity-mass relation derived by Preibisch et al. (2005a) for ONC optical sample (excluding the O-, B-, and A-type stars), $\log L_{\rm t,c} = 30.43(\pm0.04) + 1.56(\pm0.08) \times \log M$.

Thirteen and ten stars, for BN-KL and OMC-1S respectively, are added to the observed $\log L_{\rm h,c}$ to account for the missing low X-ray luminosity stars needed to match the OMC XLF (§6.1). To accomplish this, 10,000 IMF trial sets are generated where these stars are randomly distributed in the luminosity interval $26.5 \le \log L_{\rm h,c} \le 29.5$ using the formulae above in the mass interval $0.01\,{\rm M}_\odot \le M \le 0.53\,{\rm M}_\odot$. The IMF below $0.53\,{\rm M}_\odot$ is set at the average of these 10,000 trial sets. Due to uncertainties in the mass-X-ray luminosity relation, IMFs obtained in this fashion may not accurately reflect the true IMFs. However our aim here is only to compare the X-ray IMFs of different sample.

Figure 18 shows the OMC-1 core IMFs resulting from these calculations, together with the IMF of the lightly-absorbed ONC population for comparison. All three IMFs peak around $0.6\,{\rm M}_\odot$. This similarity is not surprising, as it results from our matching their XLFs and applying the same mass-X-ray luminosity relation. One can see, however, a small excess in stars with masses $M > 1$ ${\rm M}_\odot$ in the BN-KL region over both the ONC and OMC-1S samples.

6.3. Discussion

BN-KL being ten times brighter than OMC-1S, one would predict that the low-mass population should be correspondingly ten times higher. However our census of the X-ray low-mass stars show that both regions have roughly the same number of stars, $N \sim 50$. We discuss several possible explanations for this surprising result.

One possible cause could be a deficit on COUP sources in BN-KL produced by confusion in the COUP image, particularly around IRc2. Figure 2 shows a compact cluster of about 10 X-ray sources in this area. However, patchy diffuse emission is seen. It may be due in part to extended point spread function winds of bright ONC X-ray sources, but some intrinsic emission from deeply embedded stars, each emitting fewer counts than needed to trigger the COUP source detection algorithms (Getman et al. 2005b), is likely present. However, it is hard to imagine that dozens of missing X-ray sources are hidden in a so small region.

Another effect to explore combines two physical effects. While $L_{\rm bol}$ increases faster than linearly with mass for OB stars, there is a strongly stochastic variation in the mass of the single most massive (hence highest $L_{\rm bol}$) member of sparse stellar clusters. This latter point is well-illustrated in Fig. 1 of Bonnell & Clarke (1999) which shows a huge range in highest-mass member of sparse clusters. For example, if the mass of the most massive star of the cluster is 5 and 24 $M_\odot$, the model of Bonnell & Clarke predicts that the 10% quantile and the 50% quantile (median) of the cluster members, respectively, are both equal to 50. Thus, integrated $L_{\rm bol}$ is a poor predictor of cluster richness.

However, again it is not clear this stochastic sampling of the upper IMF can account for BN-KL and OMC-1S showing very similar stellar populations. The most massive star of OMC-1S is probably component C which exhibits colors consistent with a ZAMS A0 star (Gaume et al. 1998). In contrast, the BN-KL region suggests a scenario where the cluster luminosity is not dominated by a single massive source (once thought to be IRc2), but by a cluster of luminous sources (Gezari et al. 1998; Greenhill et al. 2004). The most luminous may be Source I with B3 V type or earlier producing $\gtrsim 3 \times 10^3\,L_\odot$. While a single massive star might emerge from stochastic sampling off a standard IMF, a cluster of intermediate-mass stars is less likely.

Thirdly, the differences in far-infrared (FIR) luminosities of these sub-regions may not, by themselves, indicate strong differences in the respective stellar populations. Carpenter et al. (2000) derive FIR estimates for a range of clusters in W3/W4/W5 along with estimates of the spectral type of the cluster's most massive star; they find no correlation between strength of FIR and the existence of massive stars. This can be explained as an evolutionary effect where extremely young hypercompact H II regions are quenched due to extinction in the FIR and "get brighter" as they get older. The BN-KL star cluster may thus be older, but not significantly richer, than the OMC-1S star cluster.

Finally, the most straightforward interpretation of Fig. 18 may be correct: the BN-KL region has a top-heavy IMF compared to both the OMC-1S and ONC populations. Top-heavy IMFs have been proposed for masses $M \gtrsim 50\,M_\odot$ in certain starburst regions and galaxies, but have not been reported for masses around 1–4 $M_\odot$ as suggested by Fig. 18.

7. Conclusions

The exceptionally deep COUP exposure of the Orion Nebula has allowed us to examine the embedded stellar populations associated with BN-KL and OMC-1S in the background OMC-1 cloud with the following results:

1. A total of 43 and 60 X-ray sources are detected in BN-KL and OMC-1S, respectively, 26 and 29 of which were previously seen in a shorter *Chandra* observation (Garmire et al. 2000). Half and one-third of the X-ray sources seen along the line-of-sight towards BN-KL and OMC-1S are likely foreground members of the Orion Nebula Cluster. Some 22 and 36 sources are obscured X-ray sources in BN-KL and OMC-1S, respectively; all but 5 and 18 of these sources have infrared stellar counterparts. Together, 22 of these new obscured X-ray sources without infrared counterparts appear to be YSOs in OMC-1. In particular, in OMC-1S, *Chandra* reveals a compact subcluster of seven new YSOs without infrared counterparts.

2. X-ray sources are located close to four luminous mid-infrared sources in BN-KL: BN, IRc3-i2, IRc2-C, and Source n. Their X-ray variability and spectral properties are typical of coronal activity of low-mass companions rather than wind emission from massive stars, so we may have detected companions rather than the massive stars themselves. However, interpretation of X-ray emission even from unobscured OB stars in the ONC is often difficult due to the frequent presence of magnetic effects even in mass star winds (Schulz et al. 2003; Stelzer et al. 2005).

3. We have investigated the region immediately surrounding BN itself in detail, using an X-ray image deconvolution to reveal a new, faint source which may be BN itself, or a low-mass companion to BN at ~ 200 AU. A nearby brighter X-ray source is definitively shown not to be BN, but it remains unexplained how a possible X-ray periodicity of ~ 8.3 days in this source may be related to the very similar periodicity seen for BN in the near-infrared. Finally, no X-ray emission was seen from the bright radio Source I, one of the likely main sources of luminosity in the region.

4. From a comparison of the hard band X-ray luminosity functions of obscured X-ray sources in BN-KL and OMC-1S with that for unobscured X-ray sources in the ONC, and applying a statistical relation linking X-ray luminosities with stellar masses in the ONC, we estimate that the true populations of obscured sources in BN-KL and OMC-1S are $\simeq$46 and 57 stars, with 90% confidence intervals of 34–71 and 42–82 stars, respectively. We discuss, without clear conclusion, possible explanations for their apparently similar populations in light of the greatly enhanced FIR radiation of BN-KL.

COUP is supported by the *Chandra* Guest Observer grant SAO GO3-4009A (E. Feigelson, PI). Further support was provided by the *Chandra* ACIS Team contract NAS8-38252.

Facility: CXO(ACIS)

A. Comments on individual COUP sources in BN-KL and OMC-1S regions

A.1. Individual COUP sources in BN-KL

COUP 518 This X-ray source is not a close binary as proposed by Garmire et al. (2000) in note *b* of their Table 2. Offset by 1.1″ from the UKIRT/MAX mid-infrared source MAX34 (N=7.4 mag) of Robberto et al. (2005).

COUP 523 Proplyd 132-221 (O'Dell & Wong 1996); see Kastner et al. (2005) for further details. Close binary source CB1 in the NICMOS 2.15 μm image of Stolovy et al. (1998). Offset by 0.8″ from the UKIRT/MAX mid-infrared source MAX35 (N=7.2 mag) of Robberto et al. (2005).

COUP 551 Proplyd 135-220 (O'Dell & Wong 1996) with a possible embedded silhouette disk (Bally et al. 2000); see Kastner et al. (2005) for further details. Faint 8.4 GHz radio source (Menten 2000, personal communication; see Garmire et al. 2000, Table 2, note *d*).

COUP 572 Offset by 0.5″ from the Gemini/TReCS mid-infrared source S11 = 137-217 (0.1 mJy at 11.7 μm) of Smith et al. (2005).

COUP 573 Proplyd 137-222 (O'Dell & Wong 1996); see Kastner et al. (2005) for further details. Protostar candidate TPSC-29 of Lada et al. (2000).

COUP 578 Close binary source CB2 in the NICMOS 2.15 μm image of Stolovy et al. (1998). Offset by 0.7″ from the UKIRT/MAX mid-infrared source MAX48 (N=6.3 mag) of Robberto et al. (2005).

COUP 579 Proplyd 138-207 (O'Dell & Wong 1996); see Kastner et al. (2005) for further details. The identification by Garmire et al. (2000) with the infrared source *g* (see note *f* in their Table 2) is a typo. Offset by 0.8″ from the the UKIRT/MAX mid-infrared source MAX46 (N=4.8 mag) of Robberto et al. (2005).

COUP 589 Associated with a methanol maser (Johnston et al. 1992). Peak brightness at 11.6 μm of 4.0 Jy arcsec^{-2} (Gezari et al. 1998).

COUP 592 Source near the readout trail, contaminated by soft photons (see Table 2).

COUP 599b Peak brightness at 11.6 μm of 121 Jy arcsec^{-2} (Gezari et al. 1998).

COUP 600 Associated with 6 water masers (Gaume et al. 1998).

COUP 620 Close binary source CB3 in the NICMOS 2.15 μm image of Stolovy et al. (1998). Offset by 0.6″ from the Gemini/TReCS mid-infrared source S15 = 143-205 (0.1 mJy at 11.7 μm) of Smith et al. (2005).

COUP 621 Tsujimoto et al. (2005) detect a 6.4 keV iron fluorescent line in the COUP spectrum of this source. Protostar candidate TPSC-43 of Lada et al. (2000).

COUP 628 Peak brightness at 11.6 μm of 7.5 Jy arcsec^{-2} (Gezari et al. 1998).

COUP 638 The hydrogen column density derived from the X-ray median energy is too high to be consistent with the optical/infrared counterpart: either the identification is wrong despite the perfect positional match or the computed X-ray median energy is inaccurate due to the faintness of the source.

COUP 639 This source is not the counterpart of the source IRc18 of Gezari et al. (1998), located 1.6″ away, as proposed by Garmire et al. (2000) in note *j* of their Table 2.

COUP 647 Tsujimoto et al. (2005) detect a 6.4 keV iron fluorescent line in the COUP X-ray spectrum of this source.

COUP 648 Faint 8.4 GHz radio source (Menten 2000, personal communication; see Garmire et al. 2000, Table 2, note *k*).

COUP 655 Close binary source CB4 in the NICMOS 2.15 μm image of Stolovy et al. (1998). Close double infrared source in Muench et al. (2002). Typo in Garmire et al. (2000), Table 2, note *m* : optical ID and *K* instead of optical ID and *V*, respectively. Protostar candidate TPSC-77 of Lada et al. (2000).

COUP 662 Coincident with a faint anonymous source in NICMOS 2.15 μm image of Stolovy et al. (1998, see their Fig. 1 at offset 11.6″, −2.0″).

COUP 670 Offset by 0.2″ from the Gemini/TReCS mid-infrared source S26 = 149-239 (0.4 mJy at 11.7 μm) of Smith et al. (2005) and by 0.5″ from the UKIRT/MAX mid-infrared source MAX66 (N=4.8 mag) of Robberto et al. (2005).

COUP 678 Coincident with a faint anonymous source both in the NICMOS 2.15 μm image of Stolovy et al. (1998, see their Fig. 1 at offsets 14.5″, −9.0″), and in the VLT/NACO 2.27 μm image of Lacombe et al. (2004, see their Fig. 2 at offsets −2.5″, 7.4″). This X-ray source is not

the counterpart of the optical source 9086 of Hillenbrand (1997) –corresponding to the near-infrared source 606 of Muench et al. (2002), and VLT source 476 of McCaughrean et al. (2005, in preparation)– as discussed in Garmire et al. (2000).

COUP 681 Coincident with a faint anonymous source both in the NICMOS 2.15 μm image of Stolovy et al. (1998, see target OMC-2C in the HST data archives) and in the VLT/NACO 2.27 μm image of Lacombe et al. (2004, see their Fig. 2 at offsets $-3.7''$, $4.5''$). In the VLT/NACO image, this source illuminates a $1''$-size fan-shape nebula oriented towards the south.

COUP 697 Offset by $0.4''$ from the Gemini/TReCS mid-infrared source S30 = 153-216 (0.5 mJy at 11.7 μm) of Smith et al. (2005) and by $0.8''$ from the UKIRT/MAX mid-infrared source MAX71 (N=4.7 mag) of Robberto et al. (2005).

COUP 698 Candidate double X-ray source in Garmire et al. (2000), Table 2, note *w*, now resolved (COUP 699 at $1.7''$ with PA 119°). Offset by $0.3''$ from the Gemini/TReCS mid-infrared source S31 = 153-225 (0.1 mJy at 11.7 μm) of Smith et al. (2005).

COUP 699 Proplyd 154-225 (O'Dell & Wong 1996); see Kastner et al. (2005) for further details. Offset by $0.7''$ from the UKIRT/MAX mid-infrared source MAX70 (N=7.0 mag) of Robberto et al. (2005).

A.2. Individual COUP sources in OMC-1S

COUP 420 Offset by $0.2''$ from the UKIRT/MAX mid-infrared source MAX18 (N=6.3 mag) of Robberto et al. (2005). Protostar candidate TPSC-74 of Lada et al. (2000).

COUP 423 Offset by $0.5''$ from the UKIRT/MAX mid-infrared source MAX19 (N=6.9 mag) of Robberto et al. (2005). Protostar candidate TPSC-32 of Lada et al. (2000).

COUP 434 Offset by $0.3''$ from the Gemini/TReCS mid-infrared source S1 = 116-421 (0.02 mJy at 11.7 μm) of Smith et al. (2005) and by $0.4''$ from the UKIRT/MAX mid-infrared source MAX20 (N=8.0 mag) of Robberto et al. (2005).

COUP 441 Protostar candidate TPSC-64 of Lada et al. (2000).

COUP 443 Proplyd 117-352 (O'Dell & Wong 1996); see Kastner et al. (2005) for further details.

COUP 465 Proplyd 121-434 (O'Dell & Wong 1996); see Kastner et al. (2005) for further details.

COUP 470 Offset by 0.4″ from the near-infrared source 302AB of Muench et al. (2002). Offset by 0.2″ from the Gemini/TReCS mid-infrared source IRS8 of Smith et al. (2004), by 0.2″ from Gemini/TReCS mid-infrared source S3 = 123-348 (0.1 mJy at 11.7 μm) of Smith et al. (2005), and by 0.4″ from the UKIRT/MAX mid-infrared source MAX28 (N=6.0 mag) of Robberto et al. (2005).

COUP 484 Protostar candidate TPSC-50 of Lada et al. (2000).

COUP 488 Offset by 0.3″ from the near-infrared source 318 of Muench et al. (2002). Offset by 0.15″ from the Gemini/TReCS mid-infrared source IRS7 of Smith et al. (2004), by 0.1″ from the Gemini/TReCS mid-infrared source S4 = 126-344 (0.2 mJy at 11.7 μm) of Smith et al. (2005), and by 0.3″ from the UKIRT/MAX mid-infrared source MAX31 (N=5.5 mag) of Robberto et al. (2005).

COUP 545 Offset by 0.1″ from the near-infrared source 327 of Muench et al. (2002). Offset by 0.1″ from Gemini/TReCS mid-infrared source IRS9 of Smith et al. (2004), by 0.1″ from the Gemini/TReCS mid-infrared source S8 = 134-340 (0.1 mJy at 11.7 μm) of Smith et al. (2005), and by 0.2″ from the UKIRT/MAX mid-infrared source MAX41 (N=6.3 mag) of Robberto et al. (2005).

COUP 554 Associated with a compact ($\sim$ 1.5″ FWHM) extended nebula in the VLT JHK_S images (McCaughrean et al. 2005, in preparation). The offset and K_S band magnitude are from the 2MASS counterpart 2MASSJ 05351356−0523552. Offset by 0.2″ from the near-infrared source 276 of Muench et al. (2002). Offset by 0.2″ from the Gemini/TReCS mid-infrared source IRS4 of Smith et al. (2004), by 0.2″ from the Gemini/TReCS mid-infrared source S10 = 136-356 (0.1 mJy at 11.7 μm) of Smith et al. (2005), and by 0.4″ from the UKIRT/MAX mid-infrared source MAX43 (N=6.3 mag) of Robberto et al. (2005). Protostar candidate TPSC-46 of Lada et al. (2000).

COUP 555 Associated with water masers (Gaume et al. 1998). Offset by 0.2″ from the near-infrared source 263 of Muench et al. (2002). Offset by 0.3″ from the Gemini/TReCS mid-infrared source IRS5 of Smith et al. (2004), by 0.3″ from the Gemini/TReCS mid-infrared source S9 = 136-360 (0.1 mJy at 11.7 μm) of Smith et al. (2005), and by 0.5″ from the UKIRT/MAX mid-infrared source MAX42 (N=6.8 mag) of Robberto et al. (2005). Protostar candidate TPSC-16 of Lada et al. (2000).

COUP 594 Associated with water masers (Gaume et al. 1998).

COUP 607 Associated with water masers (Gaume et al. 1998).

COUP 616 Proplyd 143-425 (O'Dell & Wong 1996); see Kastner et al. (2005) for further details. Offset by 0.1″ from the UKIRT/MAX mid-infrared source MAX54 (N=5.6 mag) of Robberto et al. (2005).

COUP 631 Proplyd 144-334 (O'Dell & Wong 1996); see Kastner et al. (2005) for further details. Offset by 0.2″ from the near-infrared source 350 of Muench et al. (2002). Offset by 0.2″ from the Gemini/TReCS mid-infrared counterpart IRS11 of Smith et al. (2004), by 0.2″ from the Gemini/TReCS mid-infrared source S19 = 144-334 (0.3 mJy at 11.7 μm) of Smith et al. (2005), and by 0.2″ from the UKIRT/MAX mid-infrared source MAX59 (N=5.9 mag) of Robberto et al. (2005).

COUP 632 Offset by 0.4″ from the near-infrared source 293 of Muench et al. (2002). Offset by 0.2″ from the Gemini/TReCS mid-infrared source IRS2 of Smith et al. (2004), by 0.2″ from the Gemini/TReCS mid-infrared source S20 = 144-351 (2.5 mJy at 11.7 μm) of Smith et al. (2005), and by 0.5″ from the UKIRT/MAX mid-infrared source MAX58 (N=4.0 mag) of Robberto et al. (2005). Protostar candidate TPSC-1 of Lada et al. (2000).

COUP 671 Proplyd 149-329 (O'Dell & Wong 1996); see Kastner et al. (2005) for further details.

REFERENCES

Allen, D. A. & Burton, M. G. 1993, Nature, 363, 54

Bally, J., Stark, A. A., Wilson, R. W., & Langer, W. D. 1987, ApJ, 312, L45

Bally, J., O'Dell, C. R., & McCaughrean, M. J. 2000, AJ, 119, 2919

Becklin, E. E. & Neugebauer, G. 1967, ApJ, 147, 799

Bonnell, I. A., & Clarke, C. J. 1999, MNRAS, 309, 461

Carpenter, J. M., Heyer, M. H., & Snell, R. L. 2000, ApJS, 130, 381

Churchwell, E., Wood, D. O. S., Felli, M., & Massi, M. 1987, ApJ, 321, 516

Dougados, C., Léna, P., Ridgway, S. T., Christou, J. C., & Probst, R. G. 1993, ApJ, 406, 112

Feigelson, E. D. & Nelson, P. I. 1985, ApJ, 293, 192

Feigelson, E. D., Broos, P., Gaffney, J. A., Garmire, G., Hillenbrand, L. A., Pravdo, S. H., Townsley, L., & Tsuboi, Y. 2002, ApJ, 574, 258

Feigelson, E. D., Getman, K. V., Townsley, L., Garmire, G., Preibisch, T., Grosso, N., & Montmerle T. 2005, ApJS (this issue)

Feigelson, E. D. & Getman, K. V. 2005, in The Initial Mass Function: 50 Years Later, E. Corbelli et al. (eds.), Kluwer, in press

Flaccomio, E., Micela, G., Sciortino, S., Favata, F., Corbally, C., & Tomaney, A. 1999, A&A, 345, 521

Flaccomio, E., Damiani, F., Micela, G., Sciortino, S., Harnden, F. R., Murray, S. S., & Wolk, S. J. 2003, ApJ, 582, 382

Flaccomio, E., Micela, G., Sciortino, S., Feigelson, E. D., Herbst, W., Favata, F., Harnden, F. R., & Vrtilek, S. D., 2005, ApJS (this issue)

Gagné, M., Caillault, J., & Stauffer, J. R. 1995, ApJ, 445, 280

Garmire, G., Feigelson, E. D., Broos, P., Hillenbrand, L. A., Pravdo, S. H., Townsley, L., & Tsuboi, Y. 2000, AJ, 120, 1426

Garmire, G. P., Bautz, M. W., Ford, P. G., Nousek, J. A., & Ricker, G. R. 2003, Proc. SPIE, 4851, 28

Gaume, R. A., Wilson, T. L., Vrba, F. J., Johnston, K. J., & Schmid-Burgk, J. 1998, ApJ, 493, 940

Giacconi, R., Rosati, P., Tozzi, P., et al. 2001, ApJ, 551, 624

Genzel, R. & Stutzki, J. 1989, ARA&A, 27, 41

Getman, K. V., Feigelson, E. D., Grosso, N., McCaughrean, M. J., Micela, G., Broos, P., Garmire, G., & Townsley, L. 2005a, ApJS (this issue)

Getman, K. V., et al. 2005b, ApJS (this issue)

Gezari, D. Y., Backman, D. E., & Werner, M. W. 1998, ApJ, 509, 283

Gomez, M., Hartmann, L., Kenyon, S. J., & Hewett, R. 1993, AJ, 105, 1927

Greenhill, L. J., Gezari, D. Y., Danchi, W. C., Najita, J., Monnier, J. D., & Tuthill, P. G. 2004, ApJ, 605, L57

Hillenbrand, L. A. 1997, AJ, 113, 1733

Hillenbrand, L. A., Strom, S. E., Calvet, N., Merrill, K. M., Gatley, I., Makidon, R. B., Meyer, M. R., & Skrutskie, M. F. 1998, AJ, 116, 1816

Hillenbrand, L. A., Carpenter, J. M., & Skrutskie, M. F. 2001, ApJ, 547, L53

Johnston, K. J., Gaume, R., Stolovy, S., Wilson, T. L., Walmsley, C. M., & Menten, K. M. 1992, ApJ, 385, 232

Johnstone, D. & Bally, J. 1999, ApJ, 510, L49

Kastner, J. H., Franz, G., Grosso, N., Bally, J., McCaughrean, M., Getman, K. V., Feigelson, E. D., & Schulz, N. S. 2005, ApJS (this issue)

Kleinmann, D. E. & Low, F. J. 1967, ApJ, 149, L1

Ku, W. H.-M., & Chanan, G. A. 1979, ApJ, 234, L59

Lacombe, F., et al. 2004, A&A, 417, L5

Lada, C. J., Muench, A. A., Haisch, K. E., Lada, E. A., Alves, J. F., Tollestrup, E. V., & Willner, S. P. 2000, AJ, 120, 3162

Lada, C. J., Muench, A. A., Lada, E. A., & Alves, J. F. 2004, AJ, 128, 1254

Lagrange, A.-M., et al. 2004, A&A, 417, L11

Lawson, W. A., Feigelson, E. D., & Huenemoerder, D. P. 1996, MNRAS, 280, 1071

Lomb, N. R. 1976, Ap&SS, 39, 447

Lonsdale, C. J., Becklin, E. E., Lee, T. J., & Stewart, J. M. 1982, AJ, 87, 1819

Lucy, L. B. 1974, AJ, 79, 745

McCaughrean, M. J. 1988, PhD thesis, Univ. Edinburgh

McCaughrean, M. J., Rayner, J. T., Zinnecker, H., & Stauffer, J. R. 1996, in S. V. W. Beckwith et al., eds., Disks and outflows around young stars, Lecture Notes in Physics 465, 33

Mezger, P. G., Zylka, R., & Wink, J. E. 1990, A&A, 228, 95

Menten, K. M. & Reid, M. J. 1995, ApJ, 445, L157

Muench, A. A., Lada, E. A., Lada, C. J., & Alves, J. 2002, ApJ, 573, 366

Mundy, L. G., Scoville, N. Z., Baath, L. B., Masson, C. R., & Woody, D. P. 1986, ApJ, 304, L51

O'Dell, C. R. & Wong, K. 1996, AJ, 111, 846

O’Dell, C. R. 2001, ARA&A, 39, 99

O’Dell, C. R. & Doi, T. 2003, AJ, 125, 277

Preibisch, T., et al. 2005a, ApJS (this issue)

Preibisch, T., et al. 2005b, ApJS (this issue)

Richardson, W. H. 1972, Optical Society of America Journal, 62, 55

Rieke, G. H., Low, F. J., & Kleinmann, D. E. 1973, ApJ, 186, L7

Robberto, M., Beckwith, S. V. W., Panagia, N., Patel, S. G., Herbst, T. M., et al. 2005, AJ, in press [astro-ph/0412665]

Scargle, J. D. 1982, ApJ, 263, 835

Schmid-Burgk, J., Guesten, R., Mauersberger, R., Schulz, A., & Wilson, T. L. 1990, ApJ, 362, L25

Schulz, N. S., Canizares, C., Huenemoerder, D., & Tibbets, K. 2003, ApJ, 595, 365

Siess, L., Dufour, E., & Forestini, M. 2000, A&A, 358, 593

Smith, N., Bally, J., Shuping, R. Y., Morris, M., & Hayward, T. L. 2004, ApJ, 610, L117

Smith, N., Bally, J., et al. 2005, ApJ, submitted

Stelzer, B., Huélamo, N., Hubrig, S., Zinnecker, H., & Micela, G. 2003, A&A, 407, 1067

Stelzer, B., Flaccomio, E., Montmerle, T., Micela, G., Sciortino, S., Favata, F., Preibisch, T., & Feigelson, E. D. 2005, ApJS (this issue)

Stolovy, S. R., et al. 1998, ApJ, 492, L151

Tan, J. C. 2004, ApJ, L47

Tsujimoto, M., Feigelson, E. D., Grosso, N., Micela, G., Tsuboi, Y., Favata, F., & Shang, S. 2005, ApJS (this issue)

Lupton, R., Blanton, M. R., Fekete, G., Hogg, D. W., O’Mullane, W., Szalay, A., & Wherry, N. 2004, PASP, 116, 133

Vuong, M. H., Montmerle, T., Grosso, N., Feigelson, E. D., Verstraete, L., & Ozawa, H. 2003, A&A, 408, 581

Weisskopf, M. C., Brinkman, B., Canizares, C., Garmire, G., Murray, S., & Van Speybroeck, L. P. 2002, PASP, 114, 1

Werner, M. W., Gatley, I., Becklin, E. E., Harper, D. A., Loewenstein, R. F., Telesco, C. M., & Thronson, H. A. 1976, ApJ, 204, 420

Wolk, S., Harnden, F. R., Flacommio, E., Micela, G., Favata, F., Glassgold, A. E., Shang, S., & Feigelson, E. D. 2005, ApJS (this issue)

Zapata, L. A., Rodríguez, L. F., & Kurtz, S. E., & O'Dell, C. R. 2004a, AJ, 127, 2252

Zapata, L. A., Rodríguez, L. F., Kurtz, S. E., O'Dell, C. R., & Ho, T. P. 2004b, ApJ, 610, L121

This preprint was prepared with the AAS LaTeX macros v5.2.

Table 1. *Chandra*/ACIS-I sources in BN-KL region.

Chandra/ACIS-I sources						Counterparts											
							Optical				Infrared					Radio	
COUP # (1)	G00 # (2)	α_{J2000} 5^h35^m (3)	δ_{J2000} $-5°$ (4)	Net Cts (5)	N_H cm^{-2} (6)	θ $''$ (7)	H97 # (8)	I mag (9)	M05 # (10)	K_S mag (11)	ID (12)	L mag (13)	$K-L$ mag (14)	ID (15)	MIR (16)	ID (17)	Class (18)
517	1	13.s03	22′00.″9	581	21.1	0.2	395	15.3	350	12.1	···	···	···	···	···	···	ONC
518	2	13.s05	22′15.″1	1274	21.5	0.2	9029	14.2	354	10.9	M673	10.1	0.6	a	MAX34	···	ONC
523	3	13.s18	22′21.″1	280	21.9	0.2	399b	16.8	361	10.5	M651A	9.0	1.1	b	MAX35	···	ONC
529	4	13.s24	22′09.″8	480	22.9	0.1	···	···	367	13.1	···	···	···	···	···	···	OMC
538	···	13.s37	22′26.″1	123	21.5	0.1	404	14.6	374	11.4	···	···	···	c	···	···	ONC
539	···	13.s31	22′39.″1	502	23.0	0.3†	···	···	···	···	L129	10.0	···	···	···	···	OMC
551	5	13.s53	22′19.″5	654	21.6	0.2	411	13.5	380	10.3	···	···	···	e	···	*cm*	ONC
572	7	13.s78	22′17.″4	794	22.8	0.1	···	···	395	11.5	···	···	···	aa	S11	···	OMC
573	6	13.s75	22′22.″0	280	22.0	0.1	420	13.6	394	9.6	M645	7.3	1.8	···	···	···	ONC
574	···	13.s70	22′30.″4	57	23.4	···	···	···	···	···	···	···	···	···	···	···	OMC
578	8	13.s82	22′02.″9	100	21.6‡	0.2	424	15.6	398	11.8	···	···	···	···	MAX48	···	ONC
579	9	13.s81	22′07.″0	7100	21.7	0.1	423	12.3	396	8.8	M703	8.1	0.7	h	MAX46	···	ONC
580	10	13.s84	22′09.″1	1487	22.2	0.1	···	···	400	12.1	···	···	···	···	···	···	OMC
588	···	13.s98	21′57.″9	102	22.4	0.2	···	···	406	11.3	···	···	···	···	···	···	OMC
589	···	13.s91	22′29.″9	60	23.3	0.2	···	···	406	···	D93	4.9	···	IRc3-i2	IRc3	···	OMC
590	···	13.s97	22′31.″8	356	22.6	0.2	···	···	408	10.6	···	···	···	i	···	···	OMC
591	···	13.s91	22′35.″7	22	23.5	···	···	···	···	···	···	···	···	···	···	···	OMC
592	···	13.s94	22′37.″5	35	*20.0*	0.3†	···	···	···	···	L150	8.6	···	···	···	···	OMC
599a	11	14.s08	22′22.″2	846	23.0	···	···	···	···	···	···	···	···	···	···	···	OMC
599b	···	14.s11	22′23.″0	60	23.0	0.4	···	···	416	5.1	M642	1.6	···	BN	IRc1	B	OMC
600	12	14.s09	22′36.″4	5172	21.3	0.2	432	13.0	415	9.3	L153	9.7	-0.4	k	···	R	ONC
620	···	14.s31	22′04.″4	17	22.2	0.1	436b	17.5	424	12.0	M709A	10.1	2.0	m	S15	···	ONC
621	13	14.s36	22′32.″7	3779	22.7	0.1	···	···	428	8.6	M598	5.7	3.0	n	···	L	OMC
622	···	14.s37	22′36.″0	170	22.6	0.2	9063	18.4	430	11.5	L160	10.1	1.8	p	···	···	ONC
628	···	14.s41	22′30.″4	93	23.4	0.1	···	···	430	···	D93	8.0	···	IRc2-C	IRc2	···	OMC
638	···	14.s53	22′06.″6	9	23.4⋆	0.0	442	15.3	436	11.9	···	···	···	···	···	···	ONC
639	14	14.s50	22′38.″7	1339	23.1	0.2†	···	···	···	···	L166	10.1	···	···	···	H	OMC
647	16	14.s67	22′11.″1	808	23.5	···	···	···	···	···	···	···	···	···	···	···	OMC
648	15	14.s66	22′33.″7	24413	21.5	0.2	448	12.1	443	9.1	M595	9.2	0.0	t	···	*cm*	ONC

Table 1—Continued

Chandra/ACIS-I sources						Counterparts											
							Optical			Infrared						Radio	
COUP # (1)	G00 # (2)	α_{J2000} 5^h35^m (3)	δ_{J2000} $-5°$ (4)	Net Cts (5)	N_H cm^{-2} (6)	θ $''$ (7)	H97 # (8)	I mag (9)	M05 # (10)	K_S mag (11)	ID (12)	L mag (13)	$K-L$ mag (14)	ID (15)	MIR (16)	ID (17)	Class (18)
655	17	$14^s.73$	$22'29''.7$	6329	22.9	0.2	···	···	454	10.4	M614A	7.7	···	···	···	···	OMC
656	···	$14^s.77$	$22'38''.2$	84	23.3	···	···	···	···	···	···	···	···	···	···	···	OMC
661	···	$14^s.83$	$22'23''.0$	66	20.0‡	0.1	9074	18.2	457	13.4	···	···	···	···	···	···	ONC
662	19	$14^s.90$	$22'25''.4$	3270	23.2	0.1	···	···	···	···	···	···	···	*NIC*	···	D	OMC
663	18	$14^s.87$	$22'31''.5$	1765	21.5	0.1	452	14.6	463	11.0	M603	8.9	2.2	u	···	···	ONC
669	21	$15^s.00$	$21'59''.9$	20431	21.5	0.2	457	12.5	472	9.8	M725	9.5	0.3	···	···	···	ONC
670	20	$14^s.92$	$22'39''.2$	29745	21.6	0.2	454	11.9	466	8.7	L186	7.6	1.1	v	S26	···	ONC
678	22	$15^s.10$	$22'31''.4$	614	22.9	0.1	···	···	···	···	···	···	···	*NIC*	···	···	OMC
680	23	$15^s.16$	$22'17''.4$	1384	23.2	···	···	···	···	···	···	···	···	···	···	···	OMC
681	···	$15^s.19$	$22'29''.5$	112	23.2	0.1	···	···	···	···	···	···	···	*NIC*	···	···	OMC
688	24	$15^s.21$	$22'24''.0$	1866	21.6	0.1	467	13.1	489	10.3	···	···	···	···	···	···	ONC
697	26	$15^s.35$	$22'15''.5$	5984	22.2	0.1	470	12.5	500	8.1	M671	6.8	1.2	y	S30	···	ONC
698	27	$15^s.34$	$22'25''.0$	282	21.1	0.1	9096	15.3	499	11.5	···	···	···	z	S31	···	ONC
699	27	$15^s.39$	$22'25''.4$	370	21.6	0.0	9096	15.3	505	10.6	···	···	···	···	MAX70	Z31	ONC
715	···	$15^s.59$	$22'18''.7$	43	23.4	0.3†	···	···	···	···	L217	12.8	···	···	···	···	OMC

Note. —

Col. 1: COUP identifier as used in Fig. 2.

Col. 2: Corresponding X-ray identifier from Garmire et al. (2000). All 27 X-ray sources of Garmire et al. (2000) were detected except their source 25, CXOU J053515.3-052218, for which they observed a factor 2 drop in count rate over 1 hr, before falling again 10 hr later. The non-detection by COUP suggests that this source was only visible previously due to an X-ray flare. The higher sensitivity COUP data also confirm the binarity of source 27 of Garmire et al. (2000) (separation $1.7''$, PA 119°). Conversely, their source 2 is not double. The presence of a source (COUP 426) is confirmed at the location of cluster of 5 photons detected by Garmire et al. (2000) $12''$ W and $16''$ S of BN.

Cols. 3–4: Centroid X-ray positions (equinox J2000.0) from the COUP ACIS-I image after boresight correction (RMS errors $\lesssim 0.1''$).

Col. 5: Net ACIS-I counts in the 0.5–8.0 keV energy band.

Col. 6: Logarithm of the hydrogen column density from XSPEC fits to the X-ray pulse height distribution when the source is bright enough; for weaker sources (marked with a star), the formula $\log(N_H/cm^{-2}) = 21.16 + 0.45 \times (MedE/keV)$ of Feigelson et al. (2005) is used. Sources with two distinct and statistically equivalent solutions yielding two different N_H values are marked with double daggers: the spectral fit with the lowest N_H value is given (Getman et al. 2005b). Potentially unreliable values

(see comments for individual sources in Table 2) are given in italics. Note that we assume the standard gas-to-dust ratio as measured in other star-forming regions, and thus transform directly between the X-ray-measured gas column density to the optical/infrared-measured dust extinction using the relation of Vuong et al. (2003).
Col. 7: Offset between the COUP position and that of the corresponding near-infrared source from the VLT JHK_S catalog of McCaughrean et al. (2005, in preparation). The RMS difference between the two catalogs is 0.2″ (Getman et al. 2005b). If no near-infrared counterpart is seen, then the offset to an associated L or L' source (Dougados et al. 1993; Muench et al. 2002; Lada et al. 2004) is given when marked by a dagger.
Cols. 8–9: Optical counterpart and I magnitude from Hillenbrand (1997).
Cols. 10–11: Near-infrared counterpart from the merged VLT JHK_S catalog of McCaughrean et al. 2005 (in preparation) and the K_S magnitude.
Cols. 12–13: 2.2μm counterpart and L or L' magnitudes from the catalogs of Muench et al. (2002); Lada et al. (2004); Dougados et al. (1993); 'D93' indicates that this source was only detected in the speckle imaging of Dougados et al. (1993).
Col. 14: $K_S - L$ or $K_S - L'$ color calculated from the K_S magnitude from Muench et al. (2002, FLWO dataset) and the L or L' magnitude from Muench et al. (2002); Lada et al. (2004).
Col. 15: Alternate near-infrared names: sources *a*–*z* and IRc are from Lonsdale et al. (1982) and Rieke et al. (1973), respectively; sources *aa* and *i2* are from Dougados et al. (1993); *NIC* indicates anonymous sources in NICMOS 2.15μm images of Stolovy et al. (1998).
Col. 16: Alternate mid-infrared names: IRc, MAX, and S refer to sources from Gezari et al. (1998), Robberto et al. (2005), and Smith et al. (2005), respectively.
Col. 17: Radio counterpart from Table 2 of Zapata et al. (2004a): new 3.6 cm sources start with 'Z', while *cm* indicates faint 8.4 GHz sources from Menten (2000, personal communication), as listed by Garmire et al. (2000).
Col. 18: Membership classification from Getman et al. (2005a), where 'ONC', 'OMC', and 'EG' stand for ONC source, OMC source, and extragalactic source, respectively. We extend here the 'OMC' classification to sources without optical counterpart and with $\log N_H \geq 22$, which are not classified 'EG' by (Getman et al. 2005a).

Table 2. X-ray properties of *Chandra*/ACIS-I sources in BN-KL region.

			X-ray photon statistics					X-ray spectral fitting						
									Temperature		Emission Measure		Luminosity	
COUP #	ID	Class	Net Cts	$\log P_{KS}$	*MedE* keV	*HR*2	*HR*3	N_H cm^{-2}	kT_1 keV	kT_2 keV	$\log EM_1, EM_2$ cm^{-3}		$\log L_h, L_{h,c}$ $erg\,s^{-1}$	
(1)	(2)	(3)	(4)	(5)	(6)	(7)	(8)	(9)	(10)	(11)	(12)	(13)	(14)	(15)
517	H395	ONC	581	-4.0	1.1	-0.7	-0.4	21.1	0.8	2.0	51.9	52.0	28.6	28.6
518	a	ONC	1274	-4.0	1.3	-0.5	-0.4	21.5	0.8	2.4	52.2	52.5	29.1	29.2
523	b	ONC	280	-2.9	1.5	-0.4	-0.3	21.9	0.8	3.1	52.1	51.8	28.6	28.7
529	367	OMC	480	-4.0	3.8	1.0	0.6	22.9	2.9	···	53.2	···	29.6	29.9
538	c	ONC	123	-0.9	1.2	-0.6	-0.8	21.5	1.0	···	51.6	···	27.7	27.7
539	L129	OMC	502	-4.0	4.0	0.9	0.8	23.0	3.1	···	53.3	···	29.6	30.0
551	e	ONC	654	-4.0	1.3	-0.6	-0.4	21.6	0.6	2.4	52.2	52.2	28.8	28.8
572	aa	OMC	794	-4.0	3.7	0.9	0.6	22.8	3.0	···	53.3	···	29.8	30.1
573	H420	ONC	280	-1.0	1.4	-0.5	-0.3	22.0	0.8	···	52.6	···	28.2	28.3
574	···	OMC	57	-4.0	4.8	···	1.0	23.4	15.0	···	52.2	···	28.7	29.2
578	H424	ONC	100	-0.6	3.0	-0.1	0.5	21.6‡	1.1	1.9	51.1	52.5	28.6	29.0
579	h	ONC	7100	-4.0	1.7	-0.3	-0.0	21.7	0.8	5.1	52.7	53.4	30.3	30.3
580	400	OMC	1487	-4.0	2.4	0.1	0.0	22.2	3.2	···	53.2	···	29.9	30.0
588	406	OMC	102	-0.3	1.9	0.2	-0.6	22.4	0.7	···	52.7	···	28.1	28.4
589	IRc3-i2	OMC	60	-0.4	3.7	-0.1	0.9	23.3	1.3	···	53.3	···	28.7	29.6
590	i	OMC	356	-4.0	3.1	0.5	0.3	22.6	3.0	···	52.7	···	29.3	29.5
591	···	OMC	22	-4.0	4.7	···	0.9	23.5	2.0	···	52.9	···	28.5	29.4
592	L150	OMC	35	-0.1	1.2	-0.6	-0.5	*20.0*	*2.1*	···	*51.0*	···	*27.6*	*27.6*
599a	···	OMC	846	-4.0	3.8	0.9	0.7	23.0	2.6	···	53.6	···	29.8	30.2
599b	BN	OMC	60	···	3.8	···	···	23.0	···	···	···	···	29.0	29.4
600	k	ONC	5172	-4.0	1.3	-0.6	-0.4	21.3	0.8	2.4	52.8	53.1	29.7	29.7
620	m	ONC	17	-0.0	1.6	-0.3	-0.2	22.2	1.5	···	51.4	···	27.6	27.7
621	n	OMC	3779	-4.0	3.6	0.7	0.5	22.7	3.5	···	53.9	···	30.5	30.7
622	p	ONC	170	-4.0	2.8	0.3	0.2	22.6	2.3	···	52.5	···	28.9	29.1
628	IRc2-C	OMC	93	-0.1	5.0	-0.5	1.0	23.4	6.0	···	52.8	···	29.1	29.7
638	H442	ONC	9	-0.2	4.9	···	1.0	23.4⋆	···	···	···	···	···	···
639	L166	OMC	1339	-4.0	4.0	0.8	0.8	23.1	2.4	···	53.9	···	30.1	30.5

Table 2—Continued

			X-ray photon statistics					X-ray spectral fitting						
									Temperature		Emission Measure		Luminosity	
COUP #	ID	Class	Net Cts	$\log P_{KS}$	*MedE* keV	*HR*2	*HR*3	N_H cm^{-2}	kT_1 keV	kT_2 keV	$\log EM_1, EM_2$ cm^{-3}		$\log L_h, L_{h,c}$ $erg\,s^{-1}$	
(1)	(2)	(3)	(4)	(5)	(6)	(7)	(8)	(9)	(10)	(11)	(12)	(13)	(14)	(15)
647	···	OMC	808	-4.0	5.2	···	1.0	23.5	5.5	···	53.8	···	30.1	30.7
648	t	ONC	24413	-4.0	1.5	-0.5	-0.2	21.5	0.9	3.0	53.4	53.8	30.6	30.6
655	454	OMC	6329	-4.0	3.6	0.8	0.6	22.9	2.5	···	54.3	···	30.7	31.0
656	···	OMC	84	-1.4	3.9	-0.0	0.8	23.3	1.5	···	53.3	···	28.9	29.7
661	H9074	ONC	66	-4.0	1.5	-0.5	0.2	20.0‡	4.4	···	51.0	···	27.9	27.9
662	*NIC*	OMC	3270	-4.0	4.5	0.7	0.9	23.2	4.0	···	54.2	···	30.6	31.0
663	u	ONC	1765	-4.0	1.4	-0.5	-0.2	21.5	0.8	3.5	52.4	52.6	29.4	29.5
669	H457	ONC	20431	-4.0	1.5	-0.5	-0.2	21.5	0.9	3.1	53.2	53.8	30.5	30.5
670	v	ONC	29745	-4.0	1.5	-0.4	-0.2	21.6	0.9	3.3	53.5	54.0	30.7	30.8
678	*NIC*	OMC	614	-4.0	4.1	0.6	0.8	22.9	5.2	···	53.1	···	29.8	30.0
680	···	OMC	1384	-4.0	4.7	0.9	0.9	23.2	7.2	···	53.7	···	30.2	30.6
681	*NIC*	OMC	112	-4.0	4.5	···	1.0	23.2	4.3	···	52.7	···	29.0	29.5
688	H467	ONC	1866	-2.4	1.3	-0.6	-0.5	21.6	0.7	2.0	52.7	52.8	29.4	29.4
697	y	ONC	5984	-4.0	2.5	0.2	0.1	22.2	3.6	···	53.7	···	30.4	30.5
698	z	ONC	282	-4.0	1.4	-0.5	-0.3	21.1	2.6	···	52.3	···	28.9	28.9
699	H9096	ONC	370	-4.0	1.5	-0.4	-0.4	21.6	2.1	···	52.6	···	29.1	29.1
715	L217	OMC	43	-1.2	4.3	···	0.9	23.4	1.3	···	53.3	···	28.5	29.5

Note. —

Col. 1: COUP identifier.

Col. 2: Name of optical/near-infrared/mid-infrared/radio counterpart.

Cols. 3–4: Source class based on counterparts and net counts, respectively.

Col. 5: Logarithm of the probability that the source is constant, as measured using a Kolmogorov-Smirnov 1-sample test (i.e. a value of −4.0 indicates a probablity of less than 10^{-4} that the source is constant.

Col. 6: Median energy of the source photons.

Cols. 7–8: Hardness ratios in 0.5–1.7 keV vs. 1.7–2.8 keV and [1.7–2.8] keV vs. 2.8–8.0 keV, respectively.

Col. 9: Logarithm of the hydrogen column density (see notes to Col. 6 in Table 1).

Cols. 10–11: Plasma temperatures .
Cols. 12–13: Emission measures.
Col. 14: Observed X-ray luminosity in the 2.8–8.0 keV band.
Col. 15: 2.8–8.0 keV band luminosity corrected for absorption.
Comments on individual sources:
COUP 574. Fitting procedure failed to constrain kT, that was fixed to 15 keV.
COUP 592. Source near the readout trail, contaminated by soft photons. Fitting procedure failed to constrain $N_{\rm H}$, that was fixed to 20. This low value of extinction is not consistent with the fact that this X-ray source has no optical counterpart but an IR counterpart (see Fig. 4). Luminosity values are considered not reliable, and won't be used here.
COUP 661. Fitting procedure failed to constrain $N_{\rm H}$, that was fixed to 20.

Table 3. *Chandra*/ACIS-I sources in OMC-1S.

Chandra/ACIS-I sources						Counterparts											
							Optical		Infrared							Radio	
COUP #	G00 #	α_{J2000} 5^h35^m	δ_{J2000} $-5°$	Net Cts	N_H cm^{-2}	θ $''$	H97 #	I mag	M05 #	K_S mag	ID #	L mag	$K-L$ mag	ID	MIR	ID	Class
(1)	(2)	(3)	(4)	(5)	(6)	(7)	(8)	(9)	(10)	(11)	(12)	(13)	(14)	(15)	(16)	(17)	(18)
416	···	11.28	24′16.″4	50	22.6	0.1	···	···	274	15.6	L76	12.5	1.5	···	···	···	OMC
419	···	11.31	24′26.″5	24	23.7	0.2	···	···	277	14.6	L77	14.3	0.8	···	···	···	OMC
420	···	11.32	24′38.″2	65	22.3	0.1	···	···	276	12.6	L78	9.6	3.0	···	MAX18	···	OMC
423	211	11.48	23′52.″0	429	23.2	0.2	···	···	282	13.0	L80	10.8	1.6	···	MAX19	···	OMC
425	···	11.54	23′40.″2	62	23.1	···	···	···	···	···	···	···	···	···	···	···	OMC
426	···	11.56	23′45.″3	24	23.5	0.2†	···	···	···	···	L82	12.9	···	···	···	···	OMC
434	214	11.66	24′21.″6	64	21.5	0.2	366	15.0	291	11.3	L87	10.6	0.7	···	S1	···	ONC
440	···	11.72	23′30.″6	57	23.2	0.3	···	···	297	12.6	L92	11.0	1.3	···	···	···	OMC
441	218	11.74	23′33.″5	404	23.0	0.1	···	···	299	13.9	L93	10.9	2.6	···	···	···	OMC
442	217	11.73	23′40.″4	1340	20.0	0.1	9008	14.2	296	11.3	L89	11.0	0.3	···	···	···	ONC
443	···	11.74	23′51.″8	32	21.8	0.2	368	15.3	298	12.2	L91	11.7	0.5	···	···	Z5	ONC
451	···	11.82	24′03.″9	4	22.2⋆	···	···	···	···	···	···	···	···	···	···	···	Unc
465	···	12.13	24′33.″9	35	21.6	0.2	376	16.0	316	12.9	L98	11.1	1.7	···	···	···	ONC
470	230	12.29	23′48.″1	12569	21.0	0.1	378a	12.9	323	9.6	L106	8.9	0.7	···	S3	···	ONC
471	229	12.26	24′24.″5	513	23.5	···	···	···	···	···	···	···	···	···	···	···	OMC
478	232	12.39	23′51.″7	284	22.3	0.1	···	···	327	12.2	L108	10.9	1.1	···	···	···	OMC
480	···	12.48	24′03.″5	35	23.2	0.0	···	···	329	13.9	L109	12.1	1.9	···	···	···	OMC
484	234	12.50	24′38.″1	54	22.5	0.2	···	···	330	13.2	L110	10.7	2.3	···	···	···	OMC
488	236	12.61	23′44.″1	3395	21.0	0.1	385	11.0	334	8.7	L112	7.9	0.7	···	S4	···	ONC
496	···	12.79	24′10.″6	11	23.3	···	···	···	···	···	···	···	···	···	···	···	OMC or EG?
497	···	12.71	24′26.″5	118	21.9	0.1	···	···	338	12.1	L113	10.9	1.3	···	···	···	ONC
506	···	12.85	23′42.″7	8	23.3⋆	···	···	···	···	···	···	···	···	···	···	···	OMC or EG?
507	···	12.88	23′51.″4	414	23.1	0.0†	···	···	···	···	L116	11.9	···	···	···	···	OMC
509	···	12.98	23′30.″0	40	23.4	···	···	···	···	···	···	···	···	···	···	···	OMC or EG?
510	251	12.98	23′54.″8	403	23.5	···	···	···	···	···	···	···	···	···	···	Z7	OMC
511	868	12.96	24′31.″6	21	23.6	···	···	···	···	···	···	···	···	···	···	···	OMC
532	···	13.26	23′30.″3	75	23.8	···	···	···	···	···	···	···	···	···	···	···	OMC
533	···	13.24	23′55.″4	360	22.7	0.1	···	···	365	14.2	M275	11.7	1.9	···	···	···	OMC
540	264	13.32	23′53.″1	143	21.1	0.1	9037	17.3	372	13.5	L130	12.9	···	···	···	···	ONC

Table 3—Continued

Chandra/ACIS-I sources						Counterparts											
							Optical			Infrared						Radio	
COUP # (1)	G00 # (2)	α_{J2000} 5^h35^m (3)	δ_{J2000} $-5°$ (4)	Net Cts (5)	N_H cm^{-2} (6)	θ $''$ (7)	H97 # (8)	I mag (9)	M05 # (10)	K_S mag (11)	ID # (12)	L mag (13)	$K-L$ mag (14)	ID (15)	MIR (16)	ID (17)	Class (18)
541	···	13^s.38	23′ 53″.2	60	21.5	0.1	9040	17.7	375	12.5	L131	11.3	0.7	A	···	···	ONC
545	268	13^s.45	23′ 40″.3	3103	21.4	0.1	409	12.6	378	9.5	L133	8.4	1.1	···	S8	···	ONC
553	272	13^s.54	23′ 30″.9	2323	20.6	0.1	412	14.0	381	11.1	L137	10.9	0.2	···	···	···	ONC
554	274	13^s.59	23′ 55″.3	14045	22.7	0.5	···	···	neb	10.4	L139	8.2	1.8	B	S10	136-356	OMC
555	···	13^s.55	23′ 59″.7	151	22.4	0.1	···	···	382	11.1	L138	9.8	1.6	C	S9	136-359	OMC
564	···	13^s.67	23′ 45″.2	5	23.2⋆	0.3	···	···	391	14.2	L141	11.0	3.0	···	···	···	OMC
565	275	13^s.62	24′ 25″.7	3905	21.3	0.0	417	13.9	386	11.2	L140	11.2	0.0	···	···	···	ONC
575	···	13^s.71	24′ 38″.0	12	23.0⋆	···	···	···	···	···	···	···	···	···	···	···	OMC or EG?
582	···	13^s.86	24′ 07″.1	18	23.3	···	···	···	···	···	···	···	···	···	···	···	OMC
583	288	13^s.88	24′ 26″.1	458	22.7	0.0	···	···	403	11.8	L147	9.3	···	···	···	···	OMC
594	···	13^s.97	24′ 09″.8	125	23.9	0.1	···	···	···	···	···	···	···	···	···	140-410	OMC
602	294	14^s.06	23′ 38″.4	1769	21.1	0.1	431	12.5	413	9.6	L152	9.5	0.2	···	···	···	ONC
603	···	14^s.01	24′ 28″.0	127	23.2	0.6†	···	···	···	···	L151	12.9	···	···	···	···	OMC
607	···	14^s.17	23′ 57″.0	10	23.1⋆	···	···	···	···	···	···	···	···	···	···	Z13	OMC or EG?
615	···	14^s.21	24′ 08″.2	37	23.3	···	···	···	···	···	···	···	···	···	···	···	OMC
616	300	14^s.28	24′ 24″.7	1096	21.2	0.1	437	11.8	422	9.1	L156	8.3	0.8	···	MAX54	···	ONC
631	309	14^s.40	23′ 33″.6	1990	21.5	0.1	441	12.6	432	9.3	L163	8.3	1.0	···	S19	···	ONC
632	···	14^s.40	23′ 51″.0	16	23.9	0.6†	···	···	···	···	L162	7.7	···	···	S20	144-351	OMC
633	···	14^s.40	24′ 10″.3	20	23.7	···	···	···	···	···	···	···	···	···	···	···	OMC or EG?
641	315	14^s.59	24′ 08″.0	206	23.3	···	···	···	···	···	···	···	···	···	···	···	OMC
650	···	14^s.66	23′ 28″.7	91	21.0	0.2	···	···	445	13.7	L174	13.9	-0.6	···	···	···	ONC
659	···	14^s.72	24′ 12″.5	175	23.6	···	···	···	···	···	···	···	···	···	···	···	OMC or EG?
666	326	14^s.83	23′ 46″.3	654	21.5	0.1	453	12.3	458	11.4	L181	10.6	0.9	···	···	···	ONC
667	325	14^s.82	24′ 06″.8	376	23.1	···	···	···	···	···	···	···	···	···	···	···	OMC
668	332	14^s.90	24′ 11″.7	109	21.6	0.0	9077	14.4	465	10.9	L185	10.9	···	···	···	···	ONC
671	335	14^s.94	23′ 28″.9	328	21.8	0.1	455	14.0	468	10.1	L188	9.1	1.0	···	···	Z23	ONC
672	336	14^s.96	23′ 39″.1	7564	21.4	0.1	456	12.2	470	9.4	L189	9.2	0.2	···	···	···	ONC
673	···	14^s.93	24′ 12″.9	1795	21.2	0.1	9079	15.3	467	10.7	L187	11.1	-0.6	···	···	···	ONC
674	337	14^s.98	24′ 17″.2	81	22.5	0.1	···	···	471	13.9	L190	11.9	···	···	···	···	OMC

Table 3—Continued

Chandra/ACIS-I sources						Counterparts											
							Optical		Infrared							Radio	
COUP #	G00 #	α_{J2000} 5^h35^m	δ_{J2000} $-5°$	Net Cts	N_H cm^{-2}	θ $''$	H97 #	I mag	M05 #	K_S mag	ID #	L mag	$K-L$ mag	ID	MIR	ID	Class
(1)	(2)	(3)	(4)	(5)	(6)	(7)	(8)	(9)	(10)	(11)	(12)	(13)	(14)	(15)	(16)	(17)	(18)
679	876	15^s.04	23′54″.4	40	21.0	0.1	···	···	477	12.1	L193	12.0	-0.2	···	···	···	ONC
684	340	15^s.16	23′46″.6	196	21.8	0.1	464	13.0	483	10.9	L199	10.3	0.4	···	···	···	ONC

Note. —
Cols. 1–18 are as for Table 1, with the following differences and/or additional notes:
Col. 2: All 31 ACIS-I sources of Garmire et al. (2000) were recovered in the COUP observation except their sources 330 and 874 (CXOU J053514.9−052411 and CXOU J053514.6−052350, respectively).
Cols. 12–14: *L* band magnitudes (sources with 'M') from Muench et al. (2002) and *L′* band magnitudes (sources with 'L') from Lada et al. (2004).
Col. 15: *K* band components from Gaume et al. (1998).
Col. 16: Mid-infrared counterparts MAX and S refer to Robberto et al. (2005) and Smith et al. (2005), respectively.
Col. 17: New 3.6 cm radio sources from Zapata et al. (2004a) are marked with 'Z'; new 1.3 cm radio sources from Zapata et al. (2004b) are labelled with the format 'xxx-yyy'.
Col. 18: Membership classifi cation from Getman et al. (2005a), where 'Unc' stands for uncertain case.

Table 4. X-ray properties of *Chandra*/ACIS-I sources in OMC-1S.

			X-ray photon statistics					X-ray spectral fitting						
									Temperature		Emission Measure		Luminosity	
COUP #	ID	Class	Net Cts	$\log P_{KS}$	*MedE* keV	*HR*2	*HR*3	N_H cm^{-2}	kT_1 [keV]	kT_2	$\log EM_1, EM_2$ cm^{-3}		$\log L_h, L_{h,c}$ erg s^{-1}	
(1)	(2)	(3)	(4)	(5)	(6)	(7)	(8)	(9)	(10)	(11)	(12)	(13)	(14)	(15)
416	274	OMC	50	-2.1	3.1	0.6	0.3	22.6	2.3	···	52.1	···	28.4	28.7
419	277	OMC	24	-1.0	5.2	···	1.0	23.7	1.9	···	53.2	···	28.5	29.7
420	276	OMC	65	-1.0	2.8	0.3	0.2	22.3	3.5	···	51.7	···	28.4	28.5
423	282	OMC	429	-4.0	4.7	0.8	0.9	23.2	5.8	···	53.2	···	29.7	30.2
425	···	OMC	62	-4.0	4.6	···	0.9	23.1	6.4	···	52.2	···	28.8	29.1
426	L82	OMC	24	-2.2	4.3	···	0.9	23.5	1.2	···	53.4	···	28.4	29.5
434	H366	ONC	64	-0.6	1.1	-0.7	-0.9	21.5	0.8	···	51.4	···	27.2	27.2
440	297	OMC	57	-3.3	4.8	-0.5	1.0	23.2	15.0	···	52.1	···	28.8	29.1
441	299	OMC	404	-3.4	3.9	0.9	0.7	23.0	2.6	···	53.2	···	29.5	29.9
442	H9008	ONC	1340	-4.0	1.1	-0.8	-0.5	20.0	0.8	2.3	52.2	52.2	28.9	28.9
443	H368	ONC	32	-0.5	2.4	0.2	-0.0	21.8	15.0	···	51.1	···	28.1	28.1
451	···	Unc	4	-0.1	2.2	···	1.0	22.2⋆	···	···	···	···	···	···
465	H376	ONC	35	-1.5	1.6	-0.3	-0.2	21.6	2.9	···	51.2	···	27.9	27.9
470	H378	ONC	12569	-4.0	1.2	-0.7	-0.3	21.0	0.8	2.7	53.1	53.4	30.1	30.1
471	···	OMC	513	-4.0	5.1	0.6	1.0	23.5	6.2	···	53.5	···	29.9	30.5
478	327	OMC	284	-3.1	2.4	0.3	0.0	22.3	2.5	···	52.5	···	29.0	29.2
480	329	OMC	35	-0.8	3.1	0.2	0.5	23.2	0.6	···	54.2	···	28.2	29.5
484	330	OMC	54	-2.5	2.8	0.7	0.1	22.5	2.8	···	52.0	···	28.5	28.7
488	H385	ONC	3395	-4.0	1.1	-0.7	-0.5	21.0	0.7	2.0	52.6	52.7	29.3	29.3
496	···	OMC or EG?	11	-0.4	5.2	···	1.0	23.3	15.0	···	51.6	···	28.2	28.6
497	338	ONC	118	-2.6	1.6	-0.3	-0.3	21.9	1.9	···	51.8	···	28.3	28.3
506	···	OMC or EG?	8	-0.4	4.8	···	1.0	23.3⋆	···	···	···	···	···	···
507	L116	OMC	414	-4.0	4.6	0.7	0.9	23.1	6.4	···	53.0	···	29.6	29.9
509	···	OMC or EG?	40	-1.2	5.1	···	1.0	23.4	15.0	···	52.5	···	29.0	29.5
510	Z7	OMC	403	-2.6	4.8	···	1.0	23.5	1.6	···	54.3	···	29.6	30.7
511	···	OMC	21	-4.0	4.8	···	0.9	23.6	0.9	···	54.2	···	28.3	30.1
532	···	OMC	75	-4.0	5.7	···	1.0	23.8	2.7	···	53.9	···	29.5	30.6

Table 4—Continued

			X-ray photon statistics					X-ray spectral fi tting						
									Temperature		Emission Measure		Luminosity	
COUP #	ID	Class	Net Cts	$\log P_{KS}$	*MedE* keV	*HR*2	*HR*3	N_H cm^{-2}	kT_1 [keV]	kT_2	$\log EM_1, EM_2$ cm^{-3}		$\log L_h, L_{h,c}$ erg s^{-1}	
(1)	(2)	(3)	(4)	(5)	(6)	(7)	(8)	(9)	(10)	(11)	(12)	(13)	(14)	(15)
533	365	OMC	360	-4.0	3.6	0.8	0.5	22.7	4.5	···	52.7	···	29.4	29.6
540	H9037	ONC	143	-4.0	1.2	-0.7	-0.3	21.1	1.0	5.9	51.7	51.6	28.6	28.6
541	A	ONC	60	-4.0	2.0	-0.1	-0.1	21.5	9.5	···	51.6	···	28.6	28.6
545	H409	ONC	3103	-4.0	1.4	-0.5	-0.3	21.4	0.8	3.2	52.8	53.1	29.9	29.9
553	H412	ONC	2323	-4.0	1.2	-0.7	-0.2	20.6	0.8	3.8	52.7	52.9	29.7	29.7
554	B	OMC	14045	-4.0	3.7	0.8	0.6	22.7	4.2	···	54.4	···	31.0	31.3
555	C	OMC	151	-1.8	2.7	0.3	0.1	22.4	2.5	···	52.3	···	28.8	29.0
564	391	OMC	5	-0.1	4.4	···	1.0	23.2*	···	···	···	···	···	···
565	H417	ONC	3905	-4.0	1.3	-0.6	-0.4	21.3	0.7	2.3	52.6	53.0	29.6	29.6
575	···	OMC or EG?	12	-0.9	4.1	···	0.8	23.0*	···	···	···	···	···	···
582	···	OMC	18	-2.3	5.1	···	0.8	23.3	15.0	···	51.8	···	28.4	28.8
583	403	OMC	458	-4.0	3.1	0.7	0.3	22.7	1.7	···	53.3	···	29.5	29.8
594	140-410	OMC	125	-4.0	5.9	···	1.0	23.9	11.1	···	53.3	···	29.4	30.4
602	H431	ONC	1769	-4.0	1.3	-0.6	-0.3	21.1	0.9	2.9	52.5	52.9	29.7	29.7
603	L151	OMC	127	-4.0	4.6	···	0.9	23.2	4.5	···	52.8	···	29.3	29.7
607	Z13	OMC or EG?	10	-0.1	4.4	-0.2	0.6	23.1*	···	···	···	···	···	···
615	···	OMC	37	-4.0	4.7	-1.0	1.0	23.3	5.1	···	52.2	···	28.5	29.1
616	H437	ONC	1096	-4.0	1.2	-0.6	-0.4	21.2	0.8	3.0	52.3	52.5	29.2	29.2
631	H441	ONC	1990	-4.0	1.4	-0.5	-0.3	21.5	0.9	2.3	52.5	53.0	29.7	29.7
632	L162	OMC	16	-0.5	6.1	···	1.0	23.9	15.0	···	53.0	···	28.9	30.0
633	···	OMC or EG?	20	-0.1	4.5	···	1.0	23.7	0.6	···	55.0	···	28.2	30.5
641	···	OMC	206	-4.0	4.6	0.5	0.9	23.3	2.8	···	53.2	···	29.4	30.0
650	445	ONC	91	-4.0	1.4	-0.5	-0.4	21.0	2.1	···	51.4	···	28.0	28.0
659	···	OMC or EG?	175	-2.1	5.0	-0.5	0.9	23.6	2.2	···	53.7	···	29.3	30.3
666	H453	ONC	654	-4.0	1.3	-0.6	-0.4	21.5	0.7	2.3	52.4	52.6	29.2	29.2
667	···	OMC	376	-4.0	4.3	0.6	0.9	23.1	4.4	···	53.2	···	29.7	30.1
668	H9077	ONC	109	-1.0	1.2	-0.6	-0.7	21.6	0.8	···	52.1	···	27.9	27.9

Table 4—Continued

			X-ray photon statistics					X-ray spectral fitting						
									Temperature		Emission Measure		Luminosity	
COUP #	ID	Class	Net Cts	$\log P_{KS}$	*MedE* keV	*HR*2	*HR*3	N_H cm^{-2}	kT_1 [keV]	kT_2	$\log EM_1, EM_2$ cm^{-3}		$\log L_h, L_{h,c}$ erg s^{-1}	
(1)	(2)	(3)	(4)	(5)	(6)	(7)	(8)	(9)	(10)	(11)	(12)	(13)	(14)	(15)
671	H455	ONC	328	-2.2	1.5	-0.4	-0.4	21.8	1.8	···	52.3	···	28.7	28.7
672	H456	ONC	7564	-4.0	1.4	-0.5	-0.3	21.4	0.8	2.7	53.0	53.5	30.1	30.2
673	H9079	ONC	1795	-4.0	1.4	-0.6	-0.2	21.2	1.0	5.0	52.6	52.9	29.8	29.8
674	471	OMC	81	-3.7	2.8	0.4	0.2	22.5	2.0	···	52.4	···	28.7	28.9
679	477	ONC	40	-0.4	1.2	-0.9	···	21.0	1.2	···	51.3	···	27.5	27.5
684	H464	ONC	196	-2.4	1.4	-0.4	-0.5	21.8	0.8	2.3	52.0	51.9	28.6	28.6

Note. —
Cols. 1–15 are as for Table 2.
Comments on individual sources:
COUP 440. Fitting procedure failed to constrain kT, that was fixed to 15 keV.
COUP 442. Fitting procedure failed to constrain N_H, that was fixed to 20.
COUP 443. Fitting procedure failed to constrain kT, that was fixed to 15 keV.
COUP 496. Fitting procedure failed to constrain kT, that was fixed to 15 keV.
COUP 509. Fitting procedure failed to constrain kT, that was fixed to 15 keV.
COUP 582. Fitting procedure failed to constrain kT, that was fixed to 15 keV.
COUP 632. Fitting procedure failed to constrain kT, that was fixed to 15 keV.

Table 5. Statistics of the membership classification of COUP sources in BN-KL and OMC-1S regions.

Membership classification (1)	BN-KL (2)	OMC-1S (3)
ONC	21	23
OMC	22	29
OMC or EG?	···	7
Unc.	···	1
Total	43	60
OMC + OMC or EG?	22	36
OMC + OMC or EG? with $L_{\rm h,c}$	21	32

Note. —
Column (1) provides the membership classification established by Getman et al. (2005a), where 'ONC', 'OMC', 'EG', and 'Unc', stand for ONC source, OMC source, extragalactic source, and uncertain case. We extend here the 'OMC' classification to sources without optical counterpart and with $\log N_{\rm H} \geq 22$, which are not classified 'EG' by (Getman et al. 2005a).
Columns (2) and (3) give the corresponding number of COUP sources with this membership classification for BN-KL and OMC-1S, respectively.

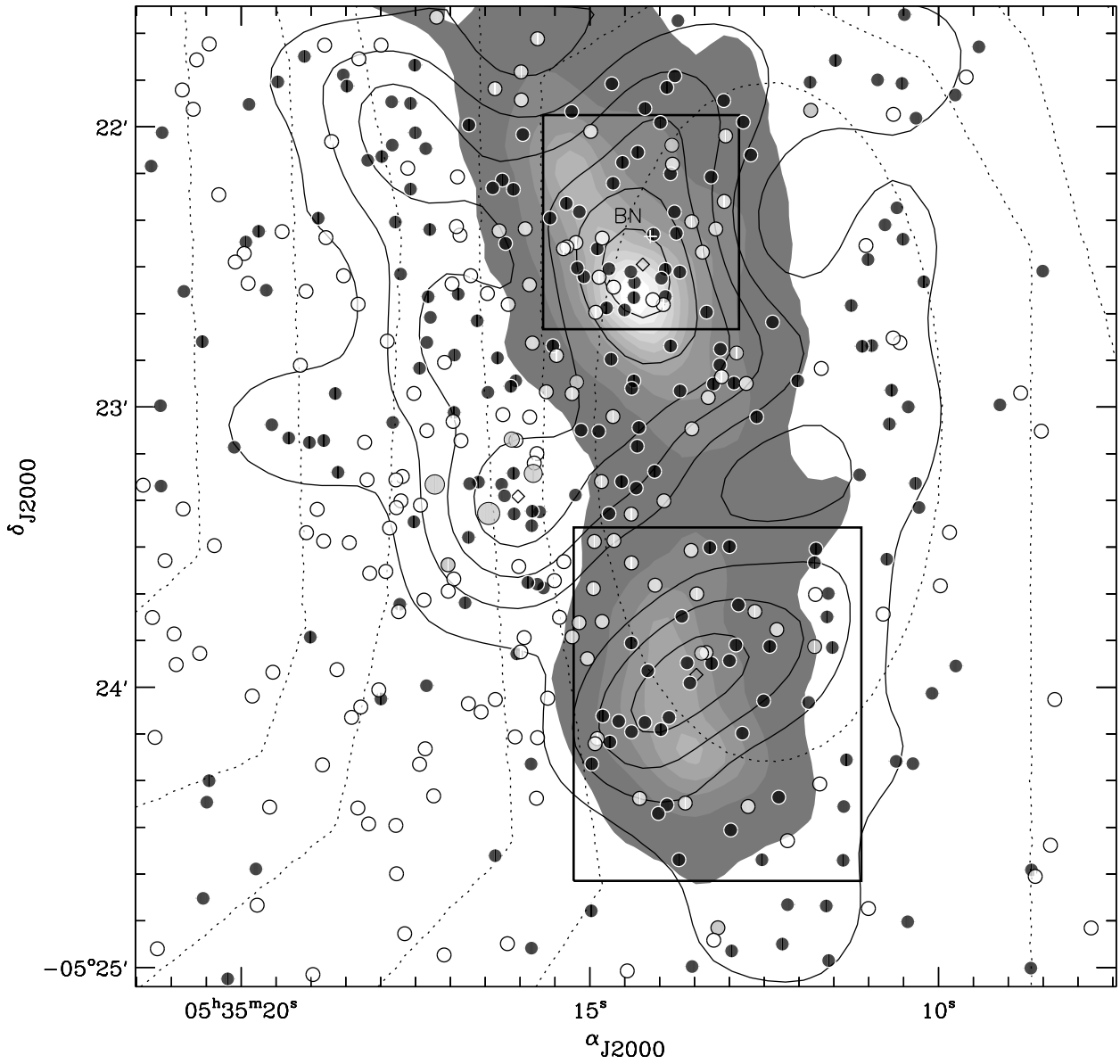

Fig. 1.— Map showing the OMC-1 areas studied in this work. The shaded contours show the SCUBA 450 μm map of Johnstone & Bally (1999), with fluxes from 45 to 450 Jy beam^{-1} in greyscale steps of 45 Jy beam^{-1}. Black and white dots mark obscured ($N_{\rm H} > 10^{22}$ cm^{-2}) and lightly-absorbed ($< 10^{22}$ cm^{-2}) COUP X-ray sources, respectively. The four brightest Trapezium OB stars, θ^1 Ori A–D, are marked by larger grey dots. Continuous contours indicate the Gaussian-smoothed surface density of the obscured COUP X-ray sources from 1000–3500 stars pc^{-2} in steps of 500 stars pc^{-2}, computed using a smoothing length of 0.025 pc (i.e. 11.5″ at 450 pc). Diamonds mark the three main density peaks: BN-KL, OMC-1S, and the Trapezium, with 3800, 2800, and 2900 stars pc^{-2}, respectively. The dotted contours show the visual extinction derived from the ^{13}CO map of Bally et al. (1987) from 20–45 mag in steps of 5 mag. The upper and lower rectangles correspond to BN-KL and OMC-1S, respectively, as studied here.

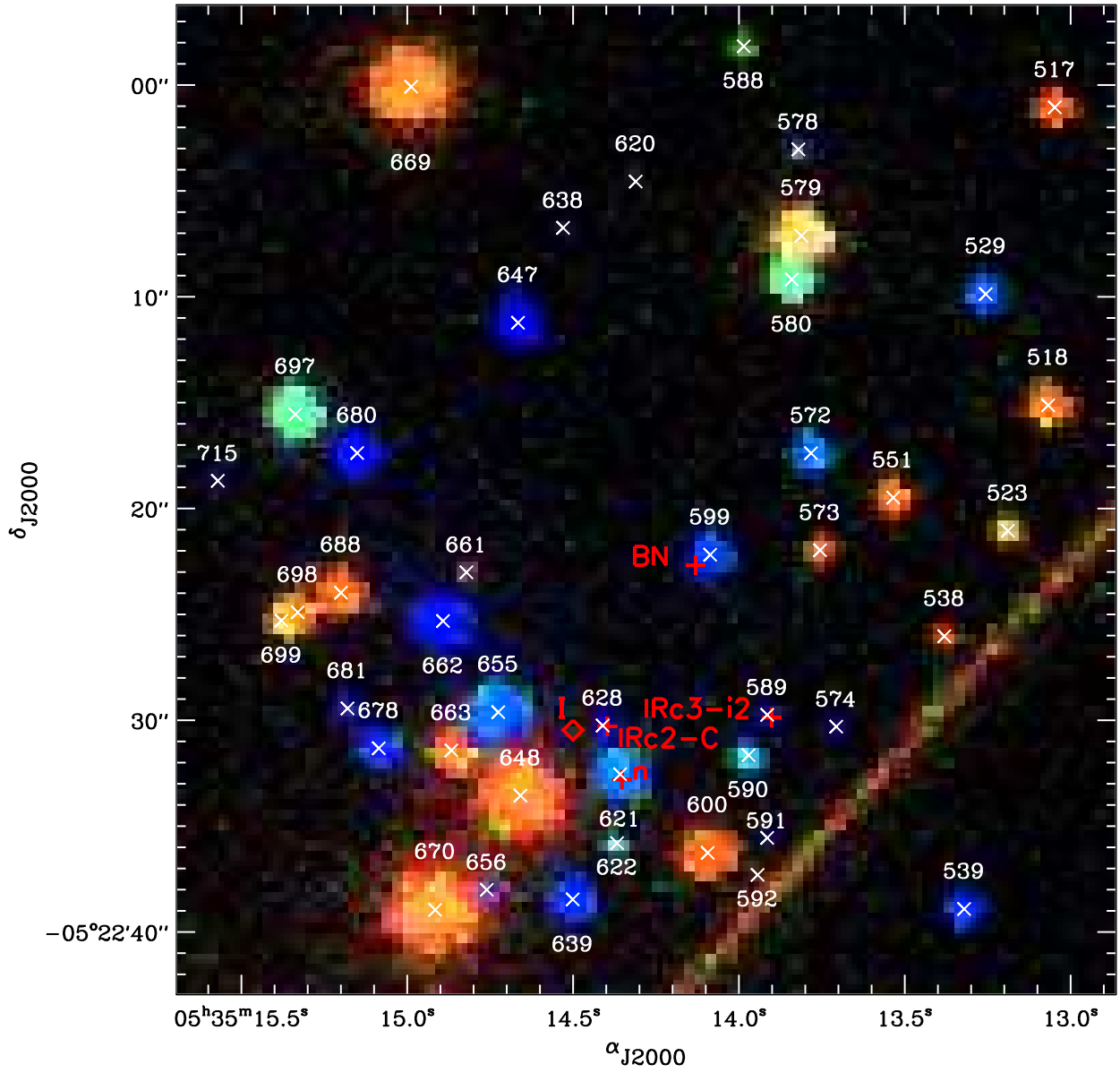

Fig. 2.— COUP view of BN-KL. Red, green, and blue represent photons in the 0.5–1.7 keV, 1.7–2.8 keV, and 2.8–8.0 keV bands, respectively, using the color-encoding scheme of Lupton et al. (2004). Red crosses mark the positions of luminous mid-infrared sources with closely associated COUP X-ray sources: BN (using the VLT J_S band position epoch 2002.0, adjusted to the mean COUP epoch of 2003.04 using the radio proper motions of Tan 2004; Menten & Reid 1995); source *n* (Gezari et al. 1998, 7.8 μm); IRc3-i2 and IRc2-C (Dougados et al. 1993, 3.6 μm). The red diamond shows the radio position of source I (Churchwell et al. 1987), which has no X-ray counterpart. The diagonal line across the lower right corner is the readout trail produced by bright X-ray source θ^1 Ori C collected during the readout of the CCD frame (so-called 'out-of-time events'). COUP catalog numbers are shown in white. Table 1 and Table 2 describe the counterparts and X-ray source properties, respectively. Comments on individual COUP sources are given in Appendix A.1.

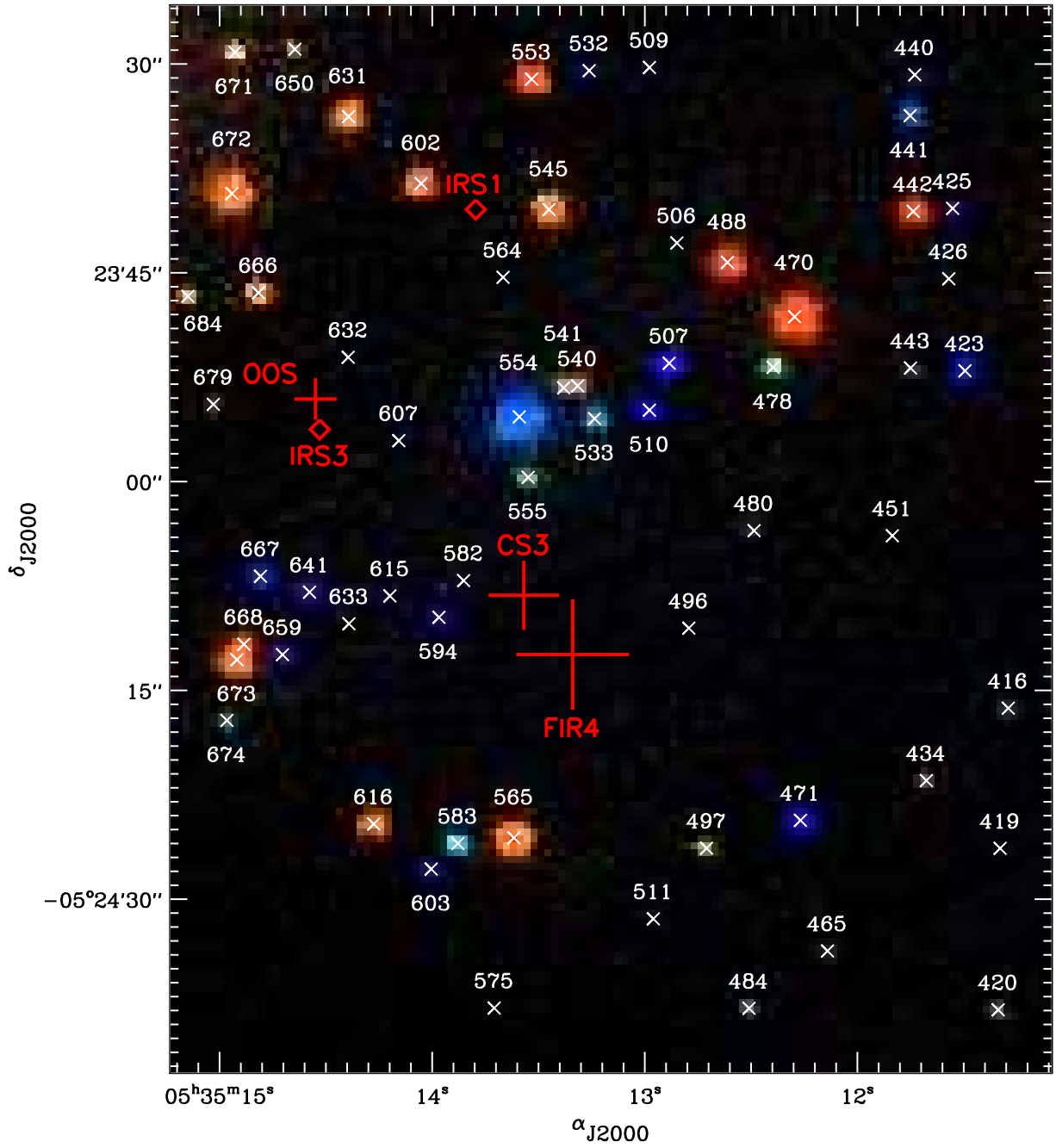

Fig. 3.— COUP view of OMC-1S, with the same color coding as for Fig. 2. Red diamonds mark the positions of IRS1 and IRS3, two bright mid-infrared sources in the region (Smith et al. 2004) without X-ray counterparts. The luminous far-infrared/sub-millimetre source FIR4 (Mezger et al. 1990), the dense molecular condensation CS3 (Mundy et al. 1986), and the hypothetical Optical Outflow Source (O'Dell & Doi 2003) are marked with red crosses. Table 3 and Table 4 describe the counterparts and X-ray source properties, respectively. Comments on individual COUP sources are given in Appendix A.2

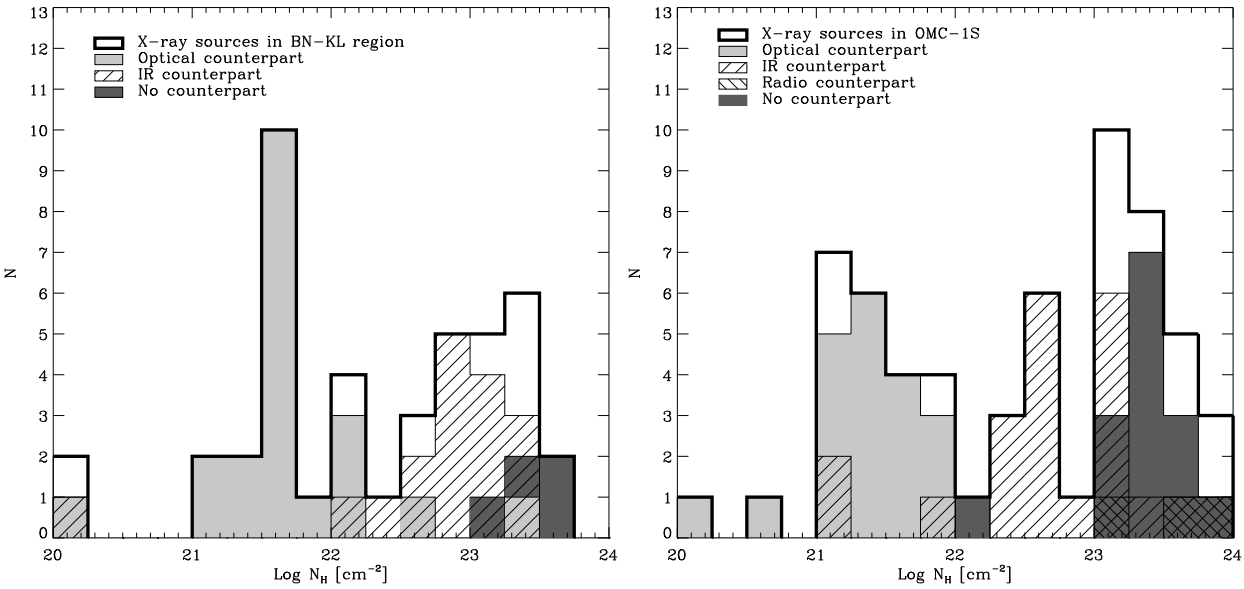

Fig. 4.— Distribution of column densities for COUP sources in BN-KL (left) and OMC-1S (right). X-ray sources with optical counterparts have the lowest column densities, while X-ray sources with near-infrared counterparts and no counterparts at all have progressively higher column densities. Two population of X-ray sources are visible: the unobscured stars of the Orion Nebula Cluster and obscured sources in the OMC-1 cores BN-KL and OMC-1S, which have column densities roughly 30 and 70 times higher, respectively.

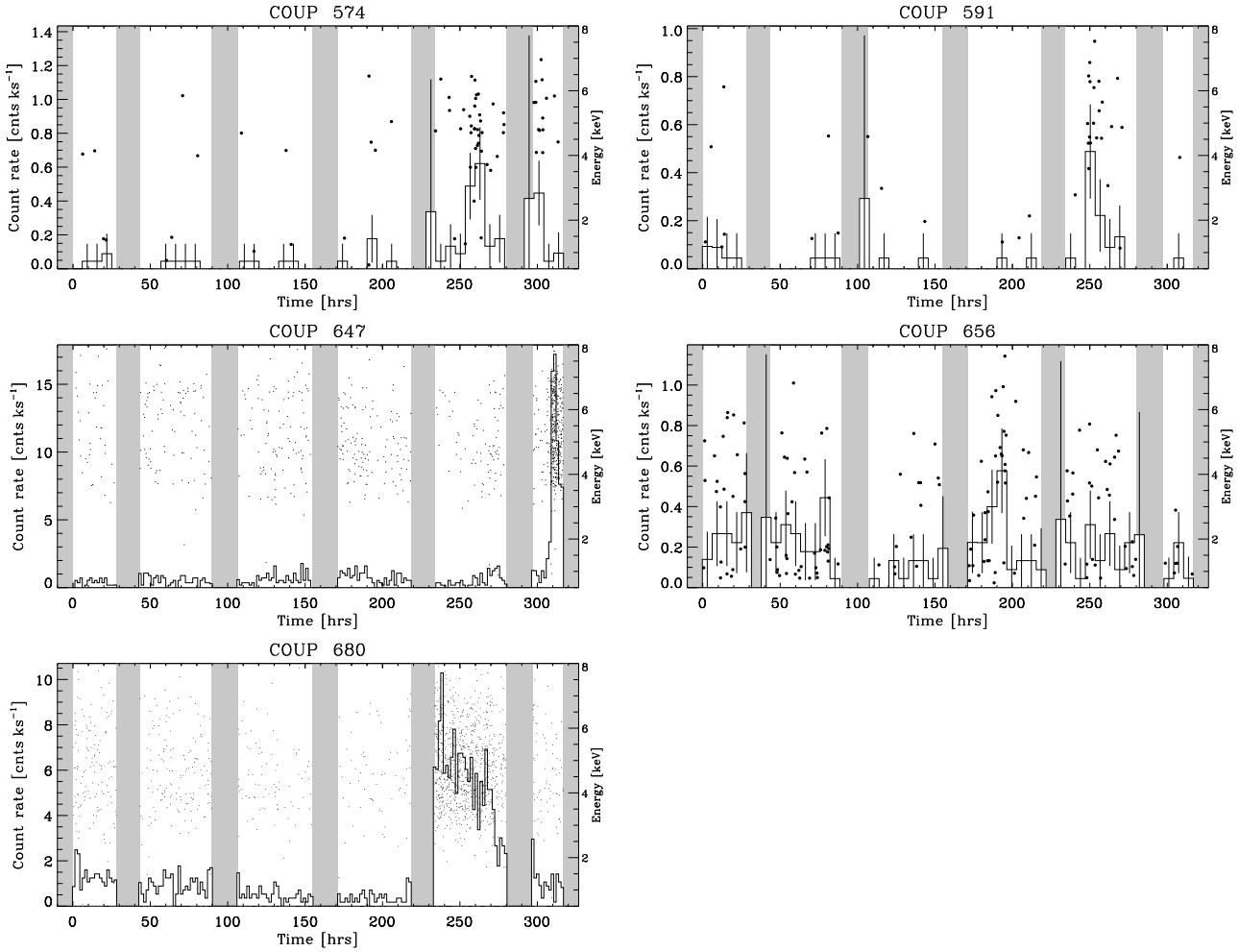

Fig. 5.— 0.5–8.0 keV light curves for COUP sources in BN-KL without infrared counterparts. Vertical grey stripes indicate the five passages of *Chandra* through the Van Allen belts where ACIS was taken out of the focal plane, and thus was not observing Orion. Dots mark the arrival times of individual X-ray photons with their corresponding energies given on the righthand axis. These obscured X-ray sources display the typical variability of young low-mass stars with X-ray flares.

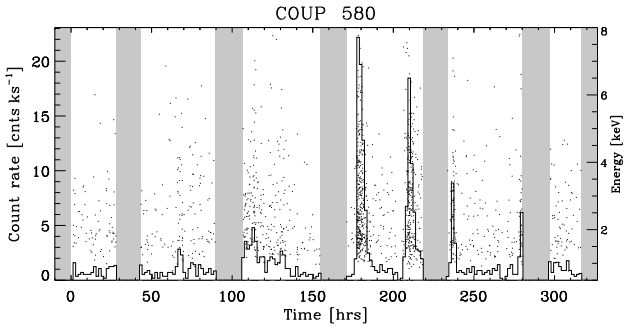

Fig. 6.— The X-ray light curve for COUP 580, highly obscured and the most variable X-ray source in BN-KL. The source displayed a remarkable series of 6 impulsive flares (peaking at 69, 113, 180, 210, 237, and 279 h during the COUP observation). The separation between each consecutive flares is 2.0, 2.7, 1.3, 1.2, and 1.7 days.

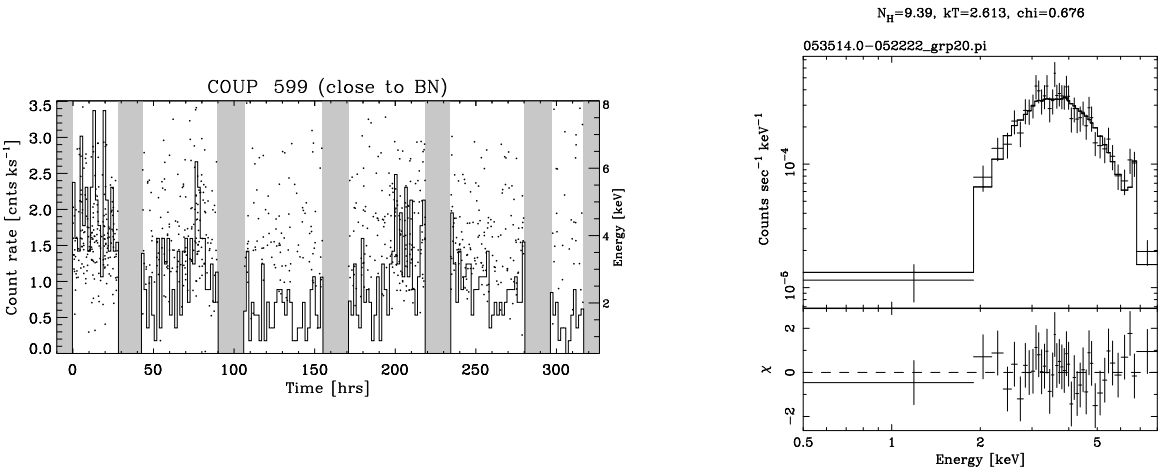

Fig. 7.— The X-ray light curve and X-ray spectrum for COUP 599a, an X-ray bright source close to (but not coincident with) BN, without an infrared counterpart.

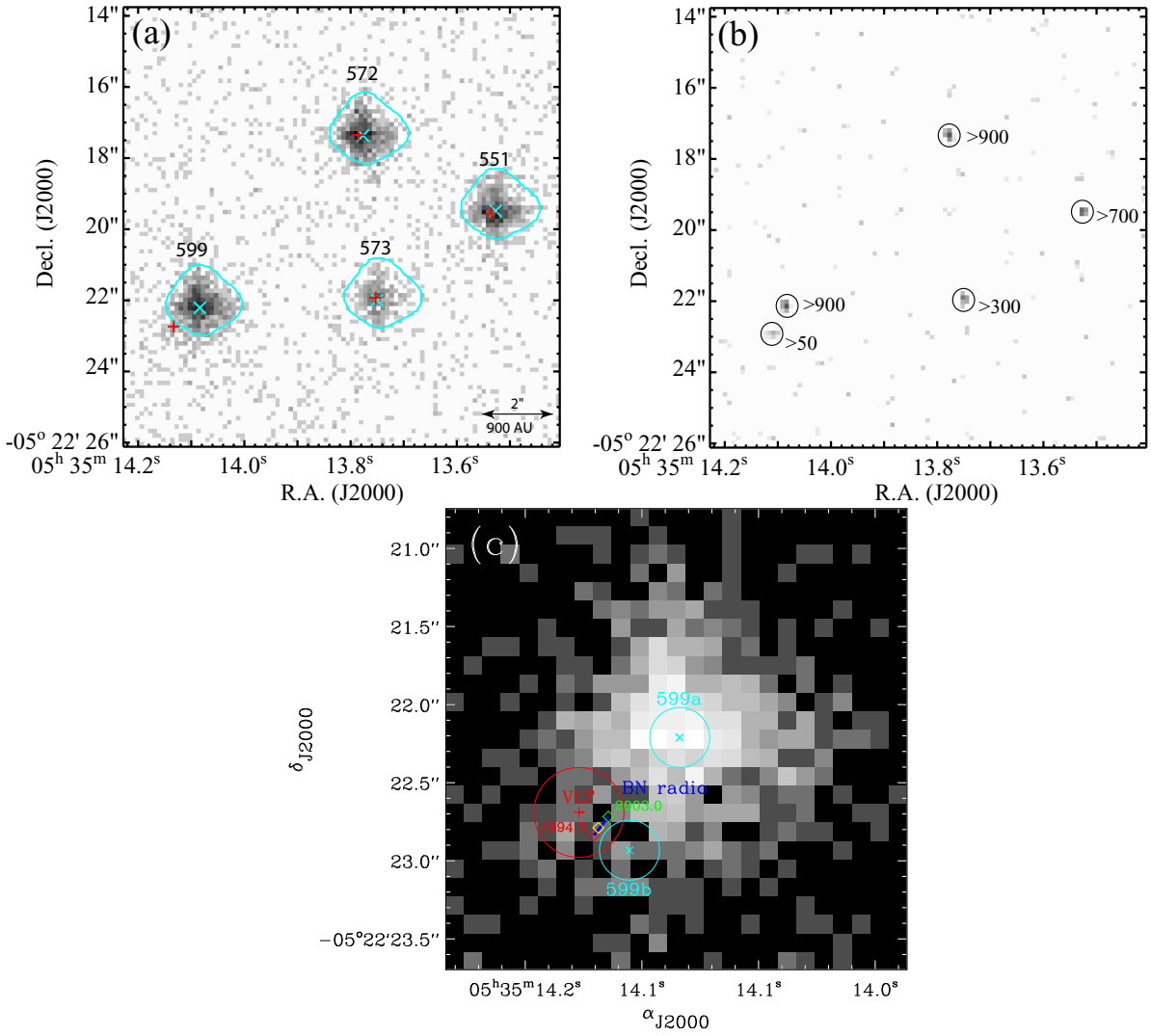

Fig. 8.— COUP images in the full 0.5–8.0 keV band covering the immediate neighborhood of BN at a finer scale of 0.125″/pixel. The image intensities are scaled logarithmically. (a) A 12.3″ × 12.3″ region of the original image; cyan crosses mark the COUP source centroids and the cyan polygons delineate the 86% enclosed energy regions, while the red crosses mark VLT JHK_S stellar positions. (b) The Maximum Likelihood reconstruction of the same field, showing the new source, COUP 599b, to the southeast of COUP 599a; the number of X-ray counts detected for each source is marked. (c) A further magnified view of the original image covering 3″ × 3″ around COUP 599a and BN. COUP 599a and COUP 599b are marked with cyan crosses and 0.2″ error circles, while the VLT J_S band position for BN is marked with a red cross and a 0.3″ error circle. The blue line shows the proper motion of the radio position of BN adjusted to the VLT frame from epoch 1994.3 (Menten & Reid 1995) to epoch 2003.04, computed from Tan (2004). The VLA positions of BN adjusted to the VLT frame are marked with red, yellow, and green diamonds, corresponding to epoch 1994.3 (Menten & Reid 1995), epoch 1994–1997 (Zapata et al. 2004a, Z12=B=BN), and COUP epoch 2003.0 (Menten & Reid 1995; Tan 2004), respectively.

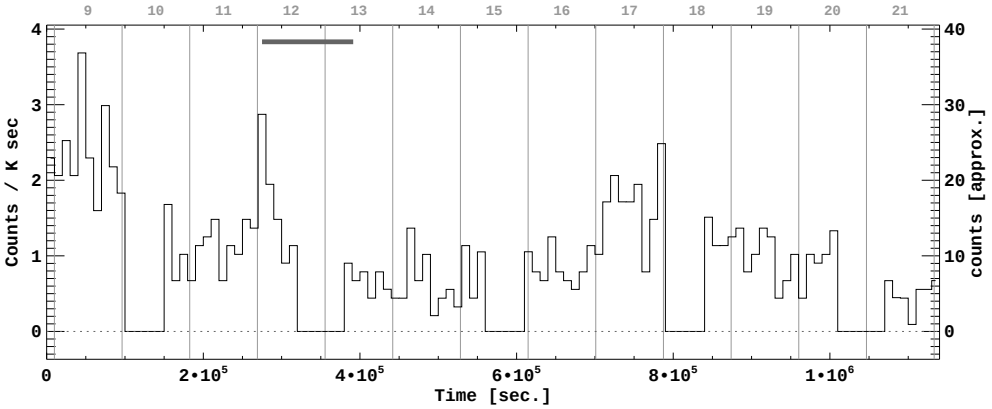

Fig. 9.— The X-ray light curve for COUP 599a in the 0.5–8.0 keV band with a coarser bin width of 10000 s. Boundaries between days in 2003 January are marked by vertical lines and the dates are displayed above the upper axis. The horizontal bar indicates the time interval that has been excluded in the Lomb-Scargle Normalized Periodogram (LNP) analysis.

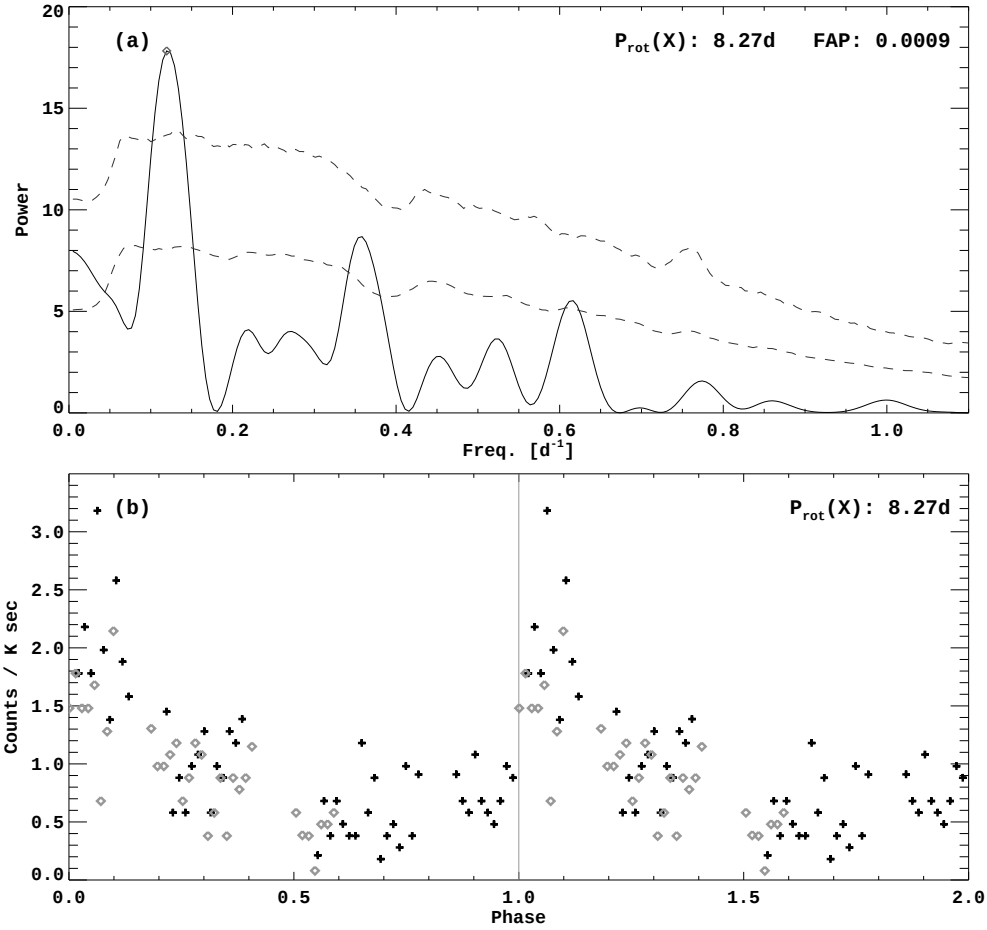

Fig. 10.— (a) Lomb-Scargle Normalized Periodogram for COUP 599a (solid line), computed from the light curve in Fig. 9 after removing the flare on 2003 January 12. Dashed lines indicate False Alarm Probability thresholds of 1% and 0.1%, calculated assuming noise with a correlation timescale of 15 h. (b) Light curve of COUP 599a folded with the period corresponding to the LNP peak, 8.27 days. Black pluses and grey diamonds indicate data points belonging to the first and the second rotational periods, respectively.

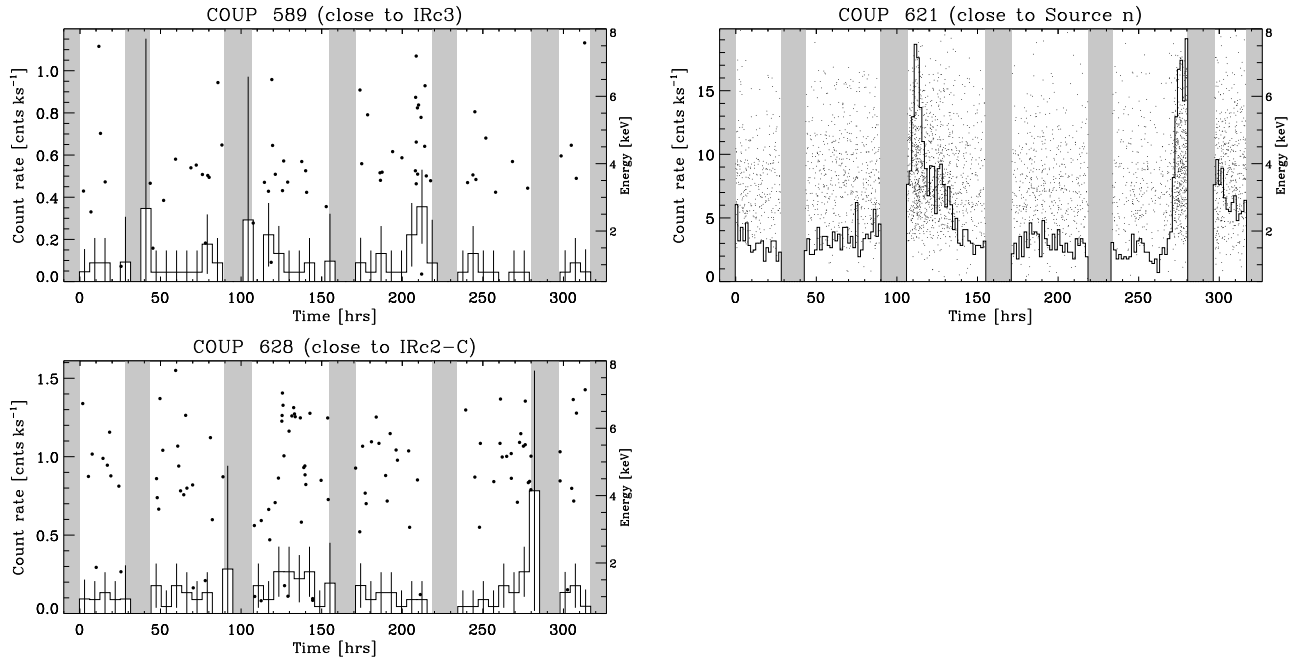

Fig. 11.— 0.5–8.0 keV band X-ray light curves for other COUP sources close to luminous mid-infrared stars in BN-KL. See Fig. 2 for the location of these sources.

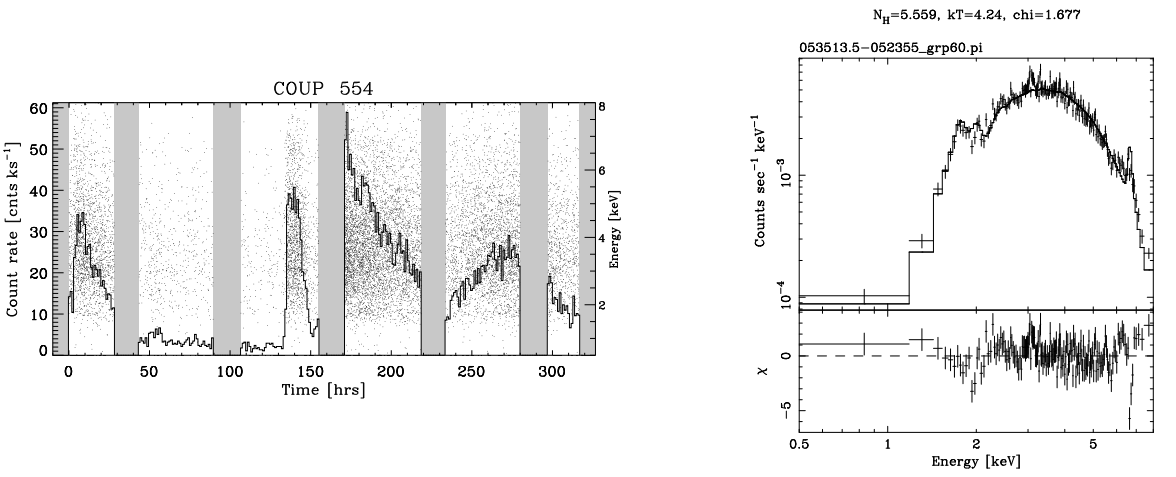

Fig. 12.— 0.5–8.0 keV band X-ray light curve and X-ray spectrum for COUP 554 in OMC-1S. This X-ray source is the brightest obscured ($\log N_{\rm H}$=22.7, i.e. $A_{\rm V} \sim 30$ mag) COUP source in OMC-1S. The near-infrared counterpart is a compact ($\sim 1.5''$ FWHM) extended reflection nebula, while the X-ray source appears to be a bona fide T Tauri star with enhanced magnetic activity.

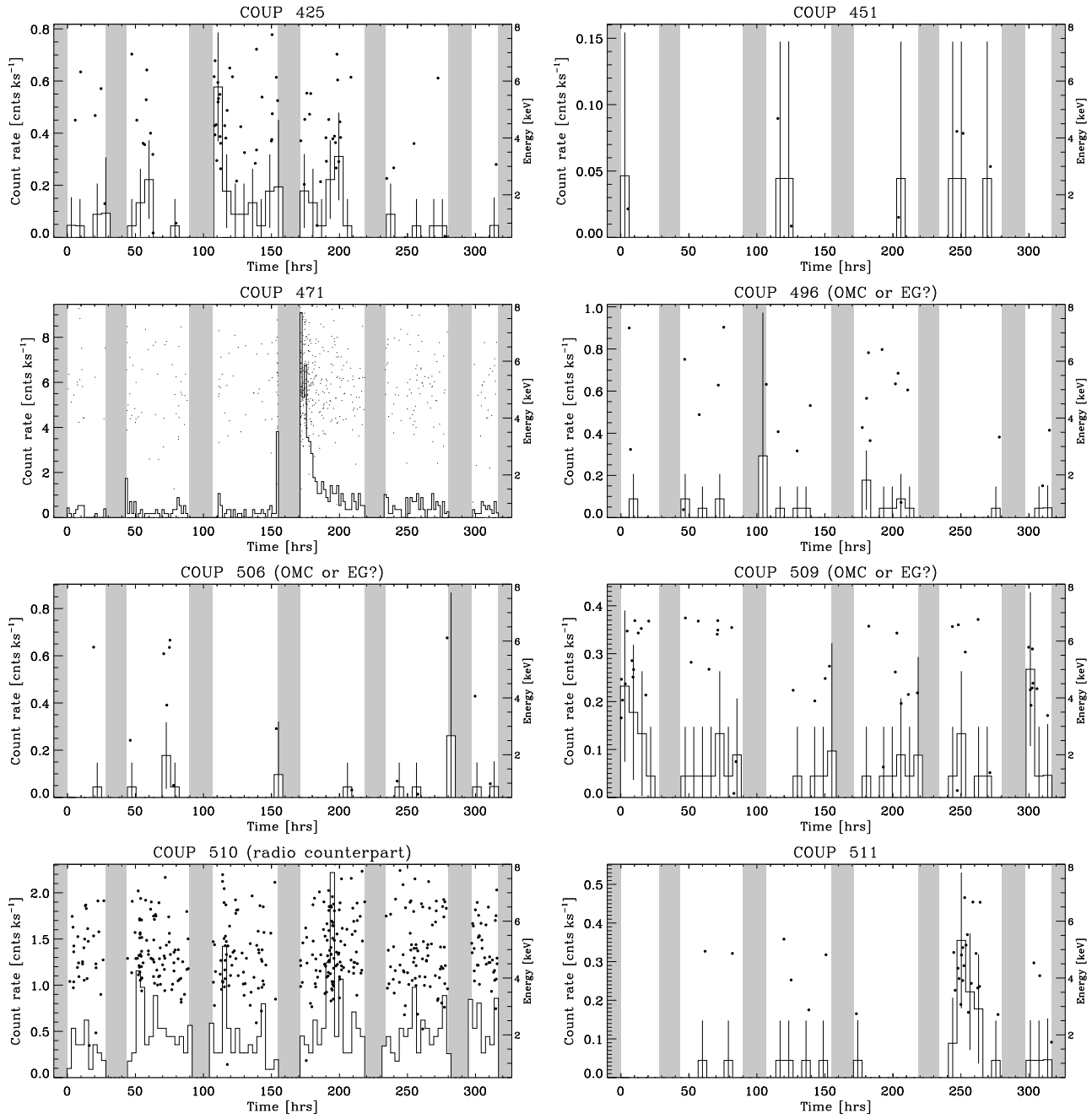

Fig. 13.— 0.5–8.0 keV light curves for COUP sources in OMC-1S without infrared counterparts. Vertical grey stripes indicate the five passages of *Chandra* through the Van Allen belts where ACIS was taken out of the focal plane, and thus was not observing Orion. Dots mark the arrival times of individual X-ray photons with their corresponding energies given on the righthand axis.

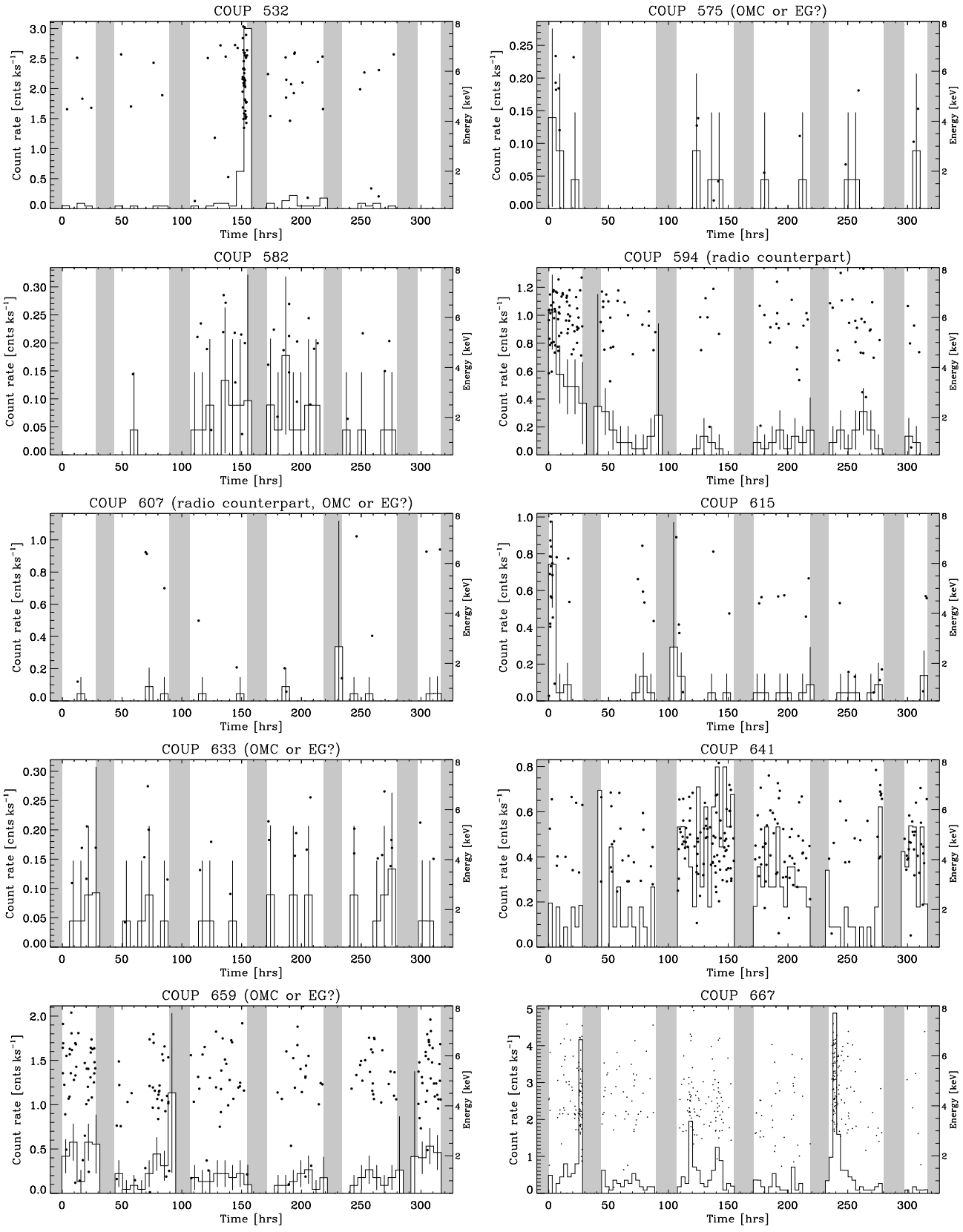

Fig. 13.— *Continued.*

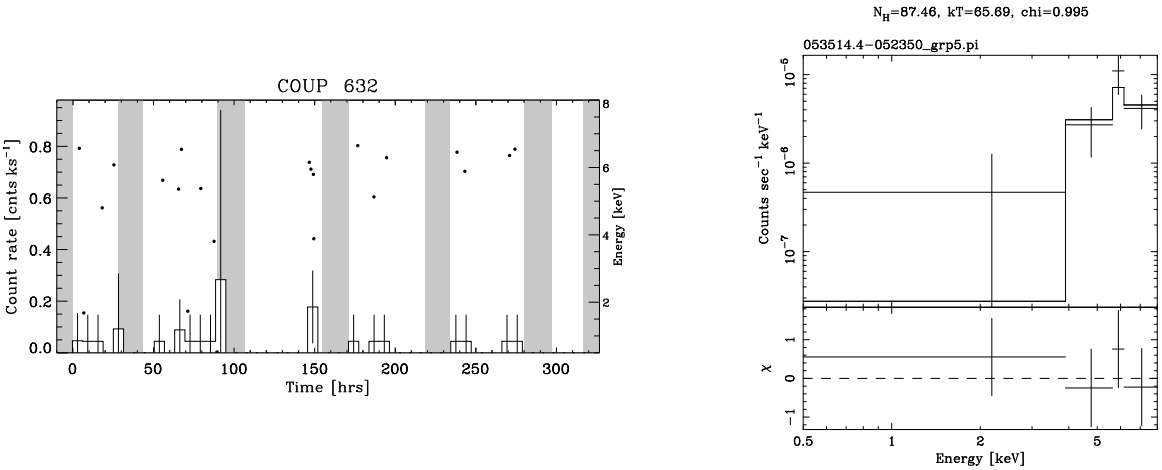

Fig. 14.— 0.5–8.0 keV band X-ray light curve and X-ray spectrum for COUP 632 in OMC-1S. This X-ray source is the most embedded COUP source with $\log N_{\rm H}$=23.94 ($A_{\rm V} \sim 500$ mag) and has a counterpart only detected in mid-infrared (Smith et al. 2004) and at 1.3 cm (Zapata et al. 2004b).

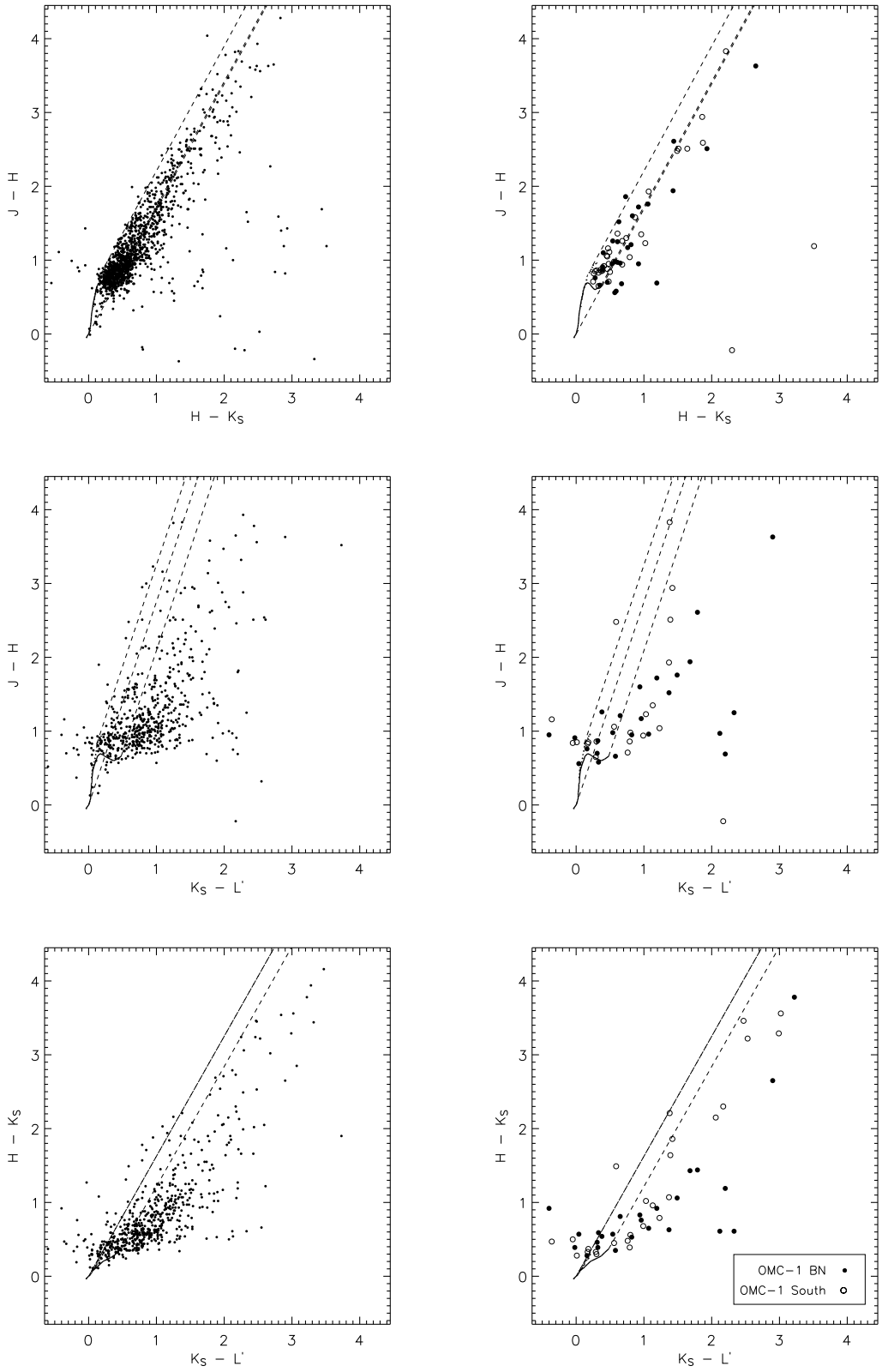

Fig. 15.— Color-color diagrams for all COUP sources (left) and the embedded OMC-1 (BN-KL and OMC-1S) sources (right).

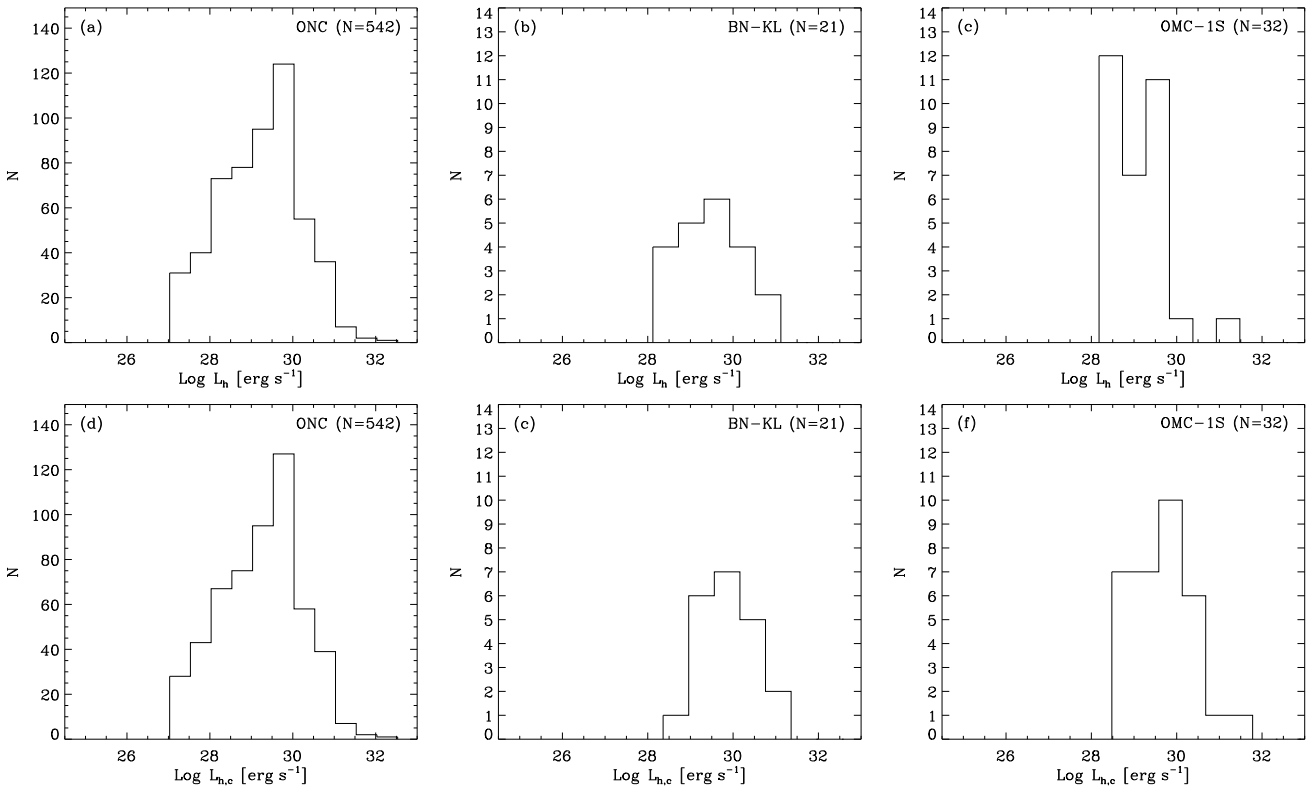

Fig. 16.— Distributions of the hard energy band (2.0–8.0 keV) X-ray luminosities for the ONC lightly-absorbed optical sample (left), obscured COUP sources in BN-KL (middle) and OMC-1S (right). The top panels show the distribution of observed luminosities, while the lower panels show the luminosities after correction for absorption. The size of each sample is given in parentheses.

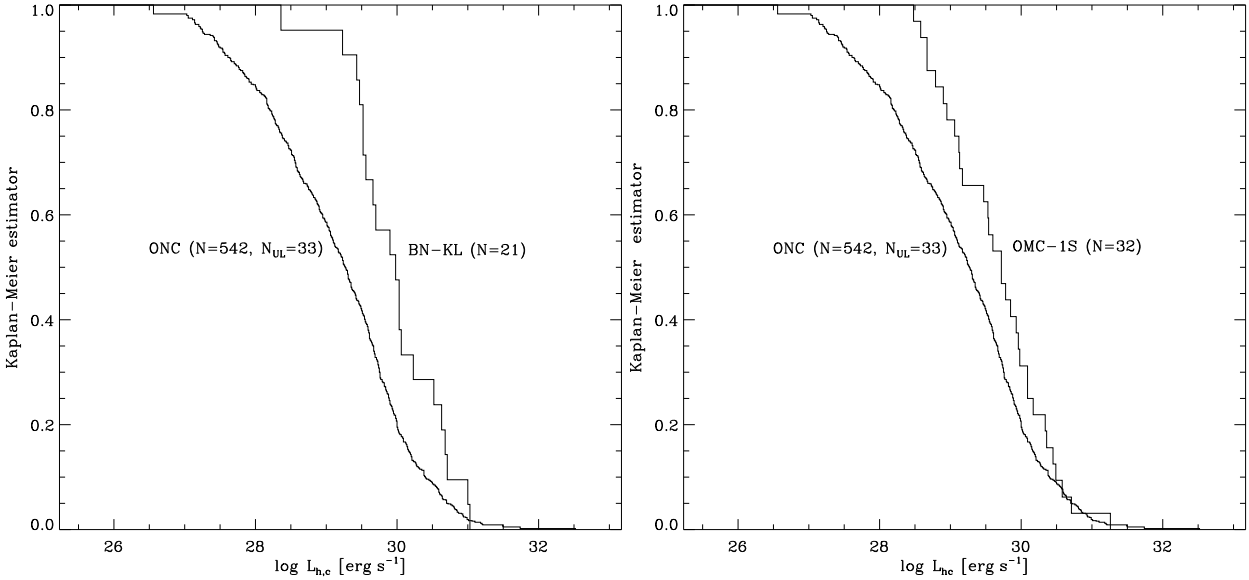

Fig. 17.— Comparison of the X-ray hard band intrinsic luminosity functions. Left: the ONC lightly-absorbed optical sample (mean=29.14±0.04, median=29.26; $N_{\rm ul}$ indicates the number of upper limits in the sample) compared with obscured COUP sources in BN-KL (mean=29.96±0.14, median=29.94). Right: the ONC lightly-absorbed optical sample compared with obscured COUP sources in OMC-1S (mean=29.66±0.12, median=29.66).

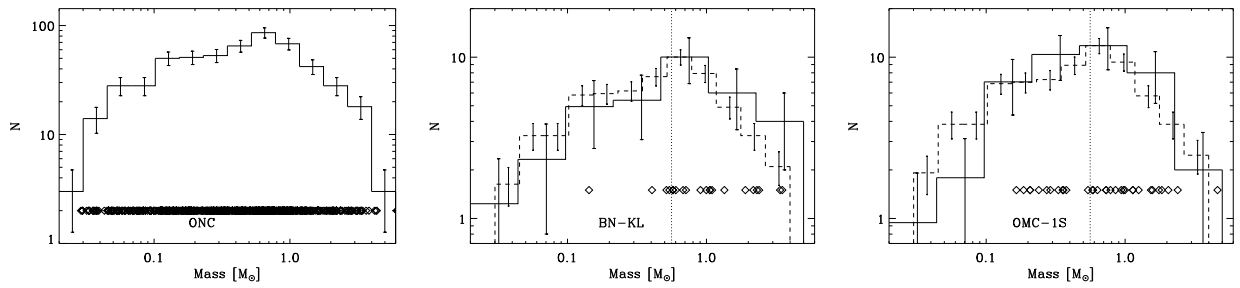

Fig. 18.— The X-ray determined Initial Mass Function for the lightly-absorbed ONC sources, and for the obscured X-ray sources in BN-KL and OMC-1S. For reference, the first panel shows the IMF of the ONC lightly-absorbed sample below $5\,M_\odot$ built from the X-ray hard band luminosities corrected for absorption. Error bars show 1σ Poisson errors. Diamonds mark the masses of the COUP sources. The samples used to construct IMFs for BN-KL and OMC-1S have been supplemented in the mass interval 0.01–$0.53\,M_\odot$ (dotted line) with 13 and 10 stars, respectively, randomly distributed to match the ONC lightly-absorbed sample; the IMFs below $\sim 0.5\,M_\odot$ are the averages of 10,000 trial sets. For comparison, the dashed line shows the IMF of the of the ONC lightly-absorbed sample normalized to the peak of the histogram.